RESEARCH ARTICLE

INTERNATIONAL RESEARCH JOURNAL OF MULTIDISCIPLINARY TECHNOVATION

Asian Research Association

DOI: 10.54392/irjmt26115

Computational Insights into the Structural, Spectroscopic, Biological, and Topological Properties of Chloro- and Fluoro-Substituted Quinolone Carboxylic Acids

A. Ram Kumar [a], A.S. Vickram [a], J. Jenifer [b], S. Selvaraj [b, *]

[a] Department of Biotechnology, Saveetha School of Engineering, Saveetha Institute of Medical and Technical Sciences (SIMATS), Chennai, 602105, Tamil Nadu, India

[b] Department of Physics, Saveetha School of Engineering, Saveetha Institute of Medical and Technical Sciences (SIMATS), Saveetha University, Chennai, 602105, Tamil Nadu, India.

* Corresponding Author Email: sselvaphy@gmail.com

DOI: https://doi.org/10.54392/irjmt26115

Received: 28-10-2025; Revised: 06-01-2026; Accepted: 17-01-2026; Published: 30-01-2026

Abstract: In this study, the quinolone derivatives (RS)-1-ethyl-5,6,8-trichloro-7-(3-methylpiperazin-1-yl)-4-oxoquinoline-3-carboxylic acid (ECMPQC) and (RS)-1-ethyl-5,6,8-trifluoro-7-(3-methylpiperazin-1-yl)-4-oxoquinoline-3-carboxylic acid (EFMPQC) were theoretically investigated using density functional theory (DFT) at the B3LYP/6-31G(d,p) level to determine their structural and spectroscopic properties. Time-dependent density functional theory (TD-DFT) was employed to analyse the frontier molecular orbitals (FMOs) and simulate the UV-Vis spectra of the quinolone derivatives in the gas phase. Natural bond orbital (NBO) and molecular electrostatic potential (MEP) analyses were carried out to elucidate intra- and intermolecular interactions as well as charge distribution characteristics. Topological analysis indicated the presence of both localized and delocalized electronic regions within the molecular frameworks. Furthermore, molecular docking studies were conducted to assess the potential biological interactions of these derivatives with viral proteins that play crucial roles in viral replication, disease progression, host mortality, and overall health outcomes.

Keywords: Quinolone, DFT, Topological, Molecular docking, Mortality

1. Introduction

Over the past few decades, halogen bonding, an analogue of hydrogen bonding, has emerged as a powerful tool in medicinal chemistry. These interactions, which involve halogen atoms acting as electrophilic species and biological targets functioning as Lewis bases, have been shown to enhance molecular recognition and binding, thereby contributing significantly to advances in drug development. Among the halogen elements, fluorine and chlorine are widely incorporated into drug molecules due to their chemical stability and favourable bioavailability [1-3]. In the medicinal and food industries, fluorine-containing structures have gained attention due to their high electronegativity, enhanced bioavailability, and distinctive physical and chemical characteristics [4]. Fluorinated compounds exhibit a broad spectrum of biological activities, including antimicrobial, antiproliferative, anti-inflammatory, antimetabolic, and antidepressant effects [5, 6]. The U.S Food and Drug Administration (FDA) approved 71 novel fluorinated compounds between 2015 and 2022, underscoring the essential role of halogenated compounds in modern medicinal chemistry [7]. Following fluorine, chlorine is an electronegative halogen that plays a crucial role in the synthesis of natural products and antibiotics, such as chloramphenicol, clindamycin, griseofulvin, and vancomycin [8]. Depending on the molecular scaffold, chlorine exerts diverse electronic characteristics, such as electron-donating, electron-withdrawing, or electronically neutral behaviour [9, 10]. Compared to functional groups such as fluorine (F), methyl (CH_3), and trifluoromethyl (CF_3), chlorine can be easily incorporated into the aromatic systems [11, 12]. The incorporation of chlorine into the molecular structures often increases membrane permeability and lipophilicity, thereby enhancing absorption and distribution within biological systems [13].

Severe Acute Respiratory Syndrome Coronavirus-2 (SARS-CoV-2), a novel viral strain, exhibits approximately 79.5% and 96% sequence similarity with SARS-CoV and Bat CoV RaTG13, respectively, and is accountable for the global COVID-19 pandemic affecting the human population. SARS-CoV-2 RNA-dependent RNA polymerase (RdRp) is a key enzyme responsible for replication and transcription

of the viral genome. Due to its significant role in viral replication and its highly conserved sequence, RdRp has emerged as a prominent target in drug discovery. Several antiviral drugs, including remdesivir, molnupiravir, favipiravir, galidesivir, ribavirin, sofosbuvir, and tenofovir, have been approved or repurposed by the FDA for targeting RdRp [14]. In contrast, the SARS-CoV-2 main protease (Mpro), also known as 3-chymotrypsin-like protease, plays a critical role in viral maturation and replication by proteolytically cleaving polyproteins into functional non-structural proteins. Due to its significant role in viral replication and high-resolution crystal structures complexed with inhibitors, Mpro has emerged as a highly attractive target for drug discovery [15, 16].

Quinoline is a heterobicyclic, nitrogen-containing aromatic compound with a molecular formula of C_9H_7N, appearing as a colorless, hygroscopic liquid with a molecular weight of 129.16 g/mol. structurally, quinoline comprises a benzene ring fused with a pyridine ring. Quinoline and its derivatives have widespread biological applications such as antiproliferative, antiviral, antihypertensive, anti-inflammatory, and antimalarial properties [17, 18]. The antifungal activity of quinoline derivatives has been evaluated against yeasts and *filamentous fungi* [19]. Both experimental and theoretical spectroscopic investigations of quinoline derivatives, such as 8-chloroquinoline, quinoline-5-carboxaldehyde, 8-nitroquinoline, quinoline-7-carboxaldehyde, and 8-hydroxyquinoline betaine, have been reported earlier [20-23]. However, the spectroscopic characteristics of quinoline derivatives such as (RS)-1-ethyl-5,6,8-trichloro-7-(3-methylpiperazin-1-yl)-4-oxo-quinoline-3-carboxylic acid (ECMPQC) and (RS)-1-ethyl-5,6,8-trifluoro-7-(3-methylpiperazin-1-yl)-4-oxo-quinoline-3-carboxylic acid (EFMPQC) have not yet been reported in the literature. In light of this observation, the present work emphasizes the spectroscopic, structural, electronic and biological properties of quinolone derivatives ECMPQC and EFMPQC using a computational approach. As highlighted in previous studies, the DFT method is considered more reliable, precise, computationally efficient, and versatile [24, 25]. Moreover, molecular docking studies were performed to investigate the potential antiviral activity of quinolone derivatives.

2. Materials and Methods

The complete theoretical calculations for the quinolone derivatives were carried out using Gaussian 09W software, in conjunction with GaussView 6, employing the DFT/B3LYP method with the 6-31G(d,p) basis set [26–33]. Electronic properties and frontier molecular orbital (FMO) characteristics were calculated using the time-dependent density functional theory (TD-DFT) approach. The density of states (DOS) in the gas phase was generated using the GaussSum program [34–36]. Natural bond orbital (NBO) calculations were performed using NBO version 3.1 [37, 38]. Graphical visualization of the computational outputs was carried out using Chemcraft and GaussView 6 [39]. Topological properties were analyzed using the Multiwfn software [40]. In addition, biological interactions were investigated through molecular docking studies using the AutoDock tool [41]. The three-dimensional (3D) and two-dimensional (2D) interaction profiles between ECMPQC and EFMPQC and the target proteins were generated using PyMOL and LigPlot+ programs [42, 43].

3. Results and Discussion

3.1 Optimized structural parameters

The optimized molecular frameworks of quinolone derivatives EFMPQC and ECMPQC, along with atom numbering, are depicted in Fig. 1, and the corresponding structural parameters are presented in the Tables. 1 and 2, while the dihedral angles are outlined in Table S1 (Supplementary Material). The optimized structure of EFMPQC comprises three F-C and O-C bonds, one O-H and N-H bond, eight N-C bonds, fourteen C-C bonds, and sixteen C-H bonds. In addition, EFMPQC exhibited six F-C-C and C-N-C, three O-C-C and C-N-H, one C-O-H and O-C-O, ten H-C-H and N-C-H, thirteen C-C-C, eleven N-C-C and seventeen C-C-H bond angles. In contrast, ECMPQC shows a comparable set of bond lengths and bond angles, with the substitution of three C-Cl bonds in place of C-F bonds and six Cl-C-C bond angles replacing the corresponding F-C-C angles, reflecting the halogen variation within the molecular framework.

In the present investigation, the bond lengths of F1-C16, F2-C18, and F3-C20 in EFMPQC were calculated to be 1.361, 1.347, and 1.333 Å, respectively. In comparison, the bond distances of Cl1-C16, Cl2-C18, and Cl3-C20 in ECMPQC were found to be 1.758, 1.749, and 1.741 Å, respectively. The longer Cl-C bond lengths relative to F-C bonds are attributed to the larger atomic radius of chlorine and its weaker orbital overlap with carbon, whereas fluorine forms shorter and stronger bonds due to its small size and effective orbital overlap. The bond distances of O4-C22, O5-C26, and O6-C26 associated with the keto and carboxylic functional groups were calculated to be 1.225, 1.345, and 1.223 Å for EFMPQC and 1.220, 1.345, and 1.221 Å for ECMPQC, respectively. The bond distance of O5-H44 in the carboxyl group was computed at 0.973 Å for EFMPQC and 0.972 Å for ECMPQC. The bond lengths of N-C were simulated within 1.020-1.485 for EFMPQC and 1.021-1.494 Å for ECMPQC. Conversely, the C-C and C-H bond distances were found to be 1.367-1.541 Å and 1.084-1.105 Å for EFMPQC and 1.362-1.542 Å and 1.085-1.105 Å for ECMPQC, respectively.

The F-C-C bond angles in EFMPQC were calculated to lie between 115.03° and 121.08°, whereas the Cl-C-C bond angles in ECMPQC ranged from 116.08° to 121.06°.

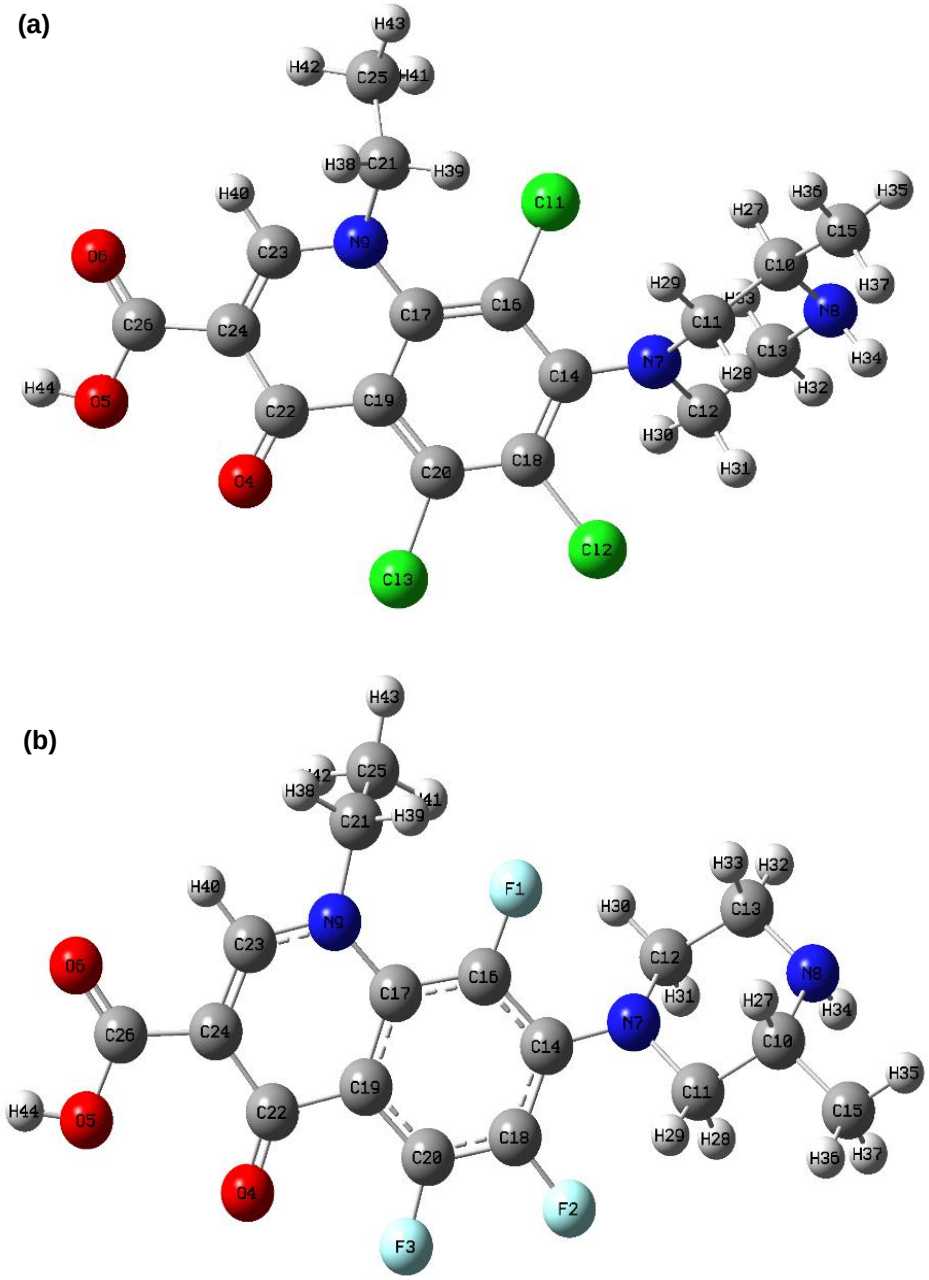

Figure 1(a). Optimized molecular structure of ECMPQC, **(b)** EFMPQC

Table 1. Optimized geometrical parameters of ECMPQC

Bond lengths (Å)	B3LYP	Bond lengths (Å)	B3LYP	Bond lengths (Å)	B3LYP
Cl1-C16	1.758	C10-C11	1.542	C16-C17	1.412
Cl2-C18	1.749	C10-C15	1.527	C17-C19	1.424
Cl3-C20	1.741	C10-H27	1.098	C18-C20	1.400
O4-C22	1.222	C11-H28	1.105	C19-C20	1.415
O5-C26	1.345	C11-H29	1.093	C19-C22	1.512
O5-H44	0.972	C12-C13	1.536	C21-C25	1.526
O6-C26	1.221	C12-H30	1.094	C21-H38	1.096
N7-C11	1.467	C12-H31	1.101	C21-H39	1.086

N7-C12	1.463	C13-H32	1.096	C22-C24	1.468
N7-C14	1.396	C13-H33	1.097	C23-C24	1.362
N8-C10	1.470	C14-C16	1.409	C23-H40	1.085
N8-C13	1.464	C14-C18	1.416	C24-C26	1.484
N8-H34	1.021	C15-H35	1.093	C25-H41	1.091
N9-C17	1.409	C15-H36	1.095	C25-H42	1.094
N9-C21	1.494	C15-H37	1.097	C25-H43	1.094
N9-C23	1.359	-	-	-	-
Bond angles (°)	**B3LYP**	**Bond angles (°)**	**B3LYP**	**Bond angles (°)**	**B3LYP**
Cl1-C16-C14	116.08	C13-N8-H34	109.01	H30-C12-H31	107.06
Cl1-C16-C17	120.04	N8-C13-C12	113.02	H32-C13-H33	107.07
Cl2-C18-C14	118.06	N8-C13-H32	108.08	C16-C14-C18	115.06
Cl2-C18-C20	119.09	N8-C13-H33	108.01	C14-C16-C17	122.04
Cl3-C20-C18	117.06	C17-N9-H21	123.01	C14-C18-C20	121.06
Cl3-C20-C19	121.06	C17-N9-C23	119.00	H35-C15-H36	108.06
O4-C22-C19	123.01	N9-C17-C16	121.05	H35-C15-H37	108.00
O4-C22-C24	123.00	N9-C17-C19	119.01	H36-C15-H37	107.07
C26-O5-H44	105.02	C21-N9-C23	114.07	C16-C17-C19	119.02
O5-C26-O6	122.01	N9-C21-C25	113.08	C17-C19-C20	118.01
O6-C26-C24	123.03	N9-C21-H38	106.08	C17-C19-C22	119.08
C11-N7-C12	114.04	N9-C21-H39	108.00	C18-C20-C19	120.08
C11-N7-C14	120.03	N9-C23-C24	124.09	C20-C19-C22	122.00
N7-C11-C10	111.01	N9-C23-H40	116.02	C19-C22-C24	113.09
N7-C11-H28	109.09	C11-C10-C15	111.05	C25-C21-H38	110.03
N7-C11-H29	109.00	C11-C10-H27	107.02	C25-C21-H39	110.08
C12-N7-C14	122.01	C10-C11-H28	109.01	C21-C25-H41	111.02
N7-C12-C13	108.07	C10-C11-H29	110.04	C21-C25-H42	112.00
N7-C12-H30	109.00	C15-C10-H27	109.01	C21-C25-H43	109.01
N7-C12-H31	111.09	C10-C15-H35	110.01	H38-C21-H39	106.08
N7-C14-C16	119.09	C10-C15-H36	111.02	C22-C24-C23	119.01
N7-C14-C18	123.04	C10-C15-H37	111.01	C22-C24-C26	125.01
C10-N8-C13	112.01	H28-C11-H29	107.03	C24-C23-H40	118.09
C10-N8-H34	108.09	C13-C12-H30	110.08	C23-C24-C26	115.03
N8-C10-C11	112.06	C13-C12-H31	108.09	H41-C25-H42	108.04
N8-C10-C15	109.09	C12-C13-H32	109.06	H41-C25-H43	108.06
N8-C10-H27	106.03	C12-C13-H33	109.03	H42-C25-H43	107.04

The C14-C16-C17 bond angle was computed to be 124.03° for EFMPQC and 122.04° for ECMPQC. Compared with ECMPQC, the bond angle in EFMPQC is increased by 1.99°, confirming the greater electronegativity of fluorine relative to chlorine, which influences angular distortion around the substituted carbon atom. The H-C-H and N-C-H bond angles for both EFMPQC and ECMPQC were found within the ranges of 106.08-108.08° and 106.03-116.02°, respectively.

Table 2. Optimized geometrical parameters of EFMPQC

Bond lengths (Å)	B3LYP	Bond lengths (Å)	B3LYP	Bond lengths (Å)	B3LYP
F1-C16	1.361	C10-C11	1.541	C16-C17	1.404
F2-C18	1.347	C10-C15	1.527	C17-C19	1.427
F3-C20	1.333	C10-H27	1.099	C18-C20	1.387
O4-C22	1.225	C11-H28	1.103	C19-C20	1.405
O5-C26	1.345	C11-H29	1.093	C19-C22	1.501
O5-H44	0.973	C12-C13	1.533	C21-C25	1.528
O6-C26	1.223	C12-H30	1.091	C21-H38	1.092
N7-C11	1.468	C12-H31	1.105	C21-H39	1.087
N7-C12	1.47	C13-H32	1.095	C22-C24	1.466
N7-C14	1.397	C13-H33	1.097	C23-C24	1.367
N8-C10	1.469	C14-C16	1.405	C23-H40	1.084
N8-C13	1.464	C14-C18	1.404	C24-C26	1.483
N8-H34	1.02	C15-H35	1.093	C25-H41	1.091
N9-C17	1.409	C15-H36	1.094	C25-H42	1.094
N9-C21	1.485	C15-H37	1.097	C25-H43	1.095
N9-C23	1.355	-	-	-	-
Bond angles (°)	**B3LYP**	**Bond angles (°)**	**B3LYP**	**Bond angles (°)**	**B3LYP**
F1-C16-C14	115.03	C13-N8-H34	109.03	H30-C12-H31	107.08
F1-C16-C17	120.04	N8-C13-C12	113.07	H32-C13-H33	107.06
F2-C18-C14	120.03	N8-C13-H32	108.09	C16-C14-C18	115.06
F2-C18-C20	117.08	N8-C13-H33	108.01	C14-C16-C17	124.03
F3-C20-C18	115.09	C17-N9-H21	124.04	C14-C18-C20	121.09
F3-C20-C19	121.08	C17-N9-C23	119.02	H35-C15-H36	108.07
O4-C22-C19	122.00	N9-C17-C16	123.00	H35-C15-H37	108.00
O4-C22-C24	124.06	N9-C17-C19	118.05	H36-C15-H37	107.06
C26-O5-H44	104.09	C21-N9-C23	116.03	C16-C17-C19	118.04
O5-C26-O6	121.07	N9-C21-C25	113.03	C17-C19-C20	117.05
O6-C26-C24	123.04	N9-C21-H38	105.06	C17-C19-C22	122.05
C11-N7-C12	113.02	N9-C21-H39	109.01	C18-C20-C19	122.03
C11-N7-C14	120.01	N9-C23-C24	126.02	C20-C19-C22	120.00
N7-C11-C10	109.06	N9-C23-H40	115.08	C19-C22-C24	113.04
N7-C11-H28	111.07	C11-C10-C15	111.03	C25-C21-H38	110.00
N7-C11-H29	108.07	C11-C10-H27	107.03	C25-C21-H39	111.04
C12-N7-C14	118.05	C10-C11-H28	109.01	C21-C25-H41	111.04
N7-C12-C13	109.06	C10-C11-H29	110.01	C21-C25-H42	111.00
N7-C12-H30	109.04	C15-C10-H27	109.01	C21-C25-H43	109.05

N7-C12-H31	110.01	C10-C15-H35	110.01	H38-C21-H39	107.01
N7-C14-C16	119.08	C10-C15-H36	111.03	C22-C24-C23	120.01
N7-C14-C18	124.05	C10-C15-H37	111.00	C22-C24-C26	125.05
C10-N8-C13	112.00	H28-C11-H29	107.05	C24-C23-H40	118.00
C10-N8-H34	108.08	C13-C12-H30	110.03	C23-C24-C26	114.04
N8-C10-C11	112.06	C13-C12-H31	109.07	H41-C25-H42	108.08
N8-C10-C15	109.09	C12-C13-H32	109.08	H41-C25-H43	107.09
N8-C10-H27	106.04	C12-C13-H33	108.05	H42-C25-H43	108.02

In addition, the O-C-C and C-C-C bond angles were calculated to be 111.03-125.05° and 122-124.06° for EFMPQC, and 111.05-125.01° and 123-123.03° for ECMPQC, respectively. The N-C-C bond angles were distributed between 109.06-126.02° for EFMPQC and 109.90-124.09° for ECMPQC. Overall, the C-C-H bond angles for both molecules were calculated to fall within the range of 107.02–118.09°.

The dihedral angles of the quinolone derivatives reveal that the F1-C16-C17-C19 and Cl1-C16-C17-C19 torsion angles in EFMPQC and ECMPQC were calculated to be -179.75° and 161.93°, respectively. In addition, the dihedral angles of C16-C14-C18-Cl2 and C18-C14-C16-Cl1 for ECMPQC were calculated to be -171.38° and -170.34°, respectively. In contrast, the dihedral angles of C16-C14-C18-F2 and C18-C14-C16-F1 for EFMPQC were found to be 178.09° and 179.29°, respectively. These results indicate that both fluorinated and chlorinated derivatives preferentially adopt antiperiplanar conformations; however, the larger deviation observed in the chlorinated derivative is attributed to the larger atomic radius of chlorine and the resulting increased steric repulsion compared to fluorine. Conversely, the fluorinated derivative exhibits enhanced conformational stability, reduced steric hindrance, and a more uniform molecular geometry.

3.2. Vibrational Analysis

The quinolone derivatives EFMPQC and ECMPQC were fully optimized, and the corresponding vibrational frequencies were calculated in the gas phase. The derivatives EFMPQC and ECMPQC consist of 44 atoms, giving rise to 126 fundamental vibrational modes, which are listed in Tables 3 and 4, and the corresponding simulated IR and Raman spectra are illustrated in Figures. 2 and 3, respectively. The theoretical spectra indicate that the characteristic absorption bands are mainly associated with stretching and deformation modes of hydroxyl (O-H), methine (C-H), keto (C=O), methyl (CH_3), methylene (CH_2), N-H, C-F, and C-Cl functional groups.

The molecular structures of EFMPQC and ECMPQC contain a single hydroxyl (O-H) group in the carboxylic acid (COOH) moiety located at the ortho position relative to the keto (C=O) group, which gives rise to stretching vibrations at 3751 cm^{-1} for ECMPQC and 3748 cm^{-1} for EFMPQC, with a potential energy distribution (PED) contribution of 100%. These values show excellent agreement with reported literature data [44]. The optimized structures of the quinolone derivatives possess two carbonyl (C=O) groups, located at the meta and para positions with respect to the ethyl (CH_2CH_3) substituent, which were calculated at 1792 and 1758 cm^{-1} for ECMPQC and 1787 and 1753 cm^{-1} for EFMPQC, respectively, showing strong correlation with reported values [45]. The N-H stretching vibrations of the piperazine ring were calculated at 3471 cm^{-1} for ECMPQC and 3475 cm^{-1} for EFMPQC, with a PED contribution of 100%, and are in good agreement with literature values [46]. The molecular structures of EFMPQC and ECMPQC contain two methine (C-H) groups, positioned ortho to the carboxyl group in the quinolone ring and adjacent to the methylene (CH_2) group in the piperazine ring. These groups contribute to stretching vibrations at 3221, 3187, 3157, and 3060 cm^{-1} for ECMPQC, and 3223, 3154, 3138, and 3095 cm^{-1} for EFMPQC, respectively, showing strong agreement with reported literature data [47].

The quinolone derivatives contain two methyl (CH_3) groups, one attached to the ethyl side chain of the quinoline ring and the other located in the piperazine ring, which contribute to both asymmetric and symmetric stretching vibrations. In the present study, the asymmetric CH_3 stretching modes were calculated at 3136, 3126, and 3110 cm^{-1} for ECMPQC, and 3138 and 3128 cm^{-1} for EFMPQC. In contrast, the symmetric CH_3 stretching modes were observed at 3062, 3047, and 3044 cm^{-1} for ECMPQC, and 3114, 3106, and 3042 cm^{-1} for EFMPQC. These values exhibit good consistency with reported literature data [48]. Furthermore, the molecular structures of the quinolone derivatives contain four methylene (CH_2) groups, which contribute to both symmetric and asymmetric stretching vibrations. The bands calculated at 3038, 2994, and 2950 cm^{-1} for ECMPQC, and 3045, 2979, and 2952 cm^{-1} for EFMPQC, correspond to symmetric CH_2 stretching modes, while the bands at 3106, 3103, and 3094 cm^{-1}

for ECMPQC, and 3185 and 3104 cm^{-1} for EFMPQC, are assigned to asymmetric stretching modes. These assignments show good agreement with reported experimental and theoretical studies [49]. The molecular structure of ECMPQC contains three C-Cl bonds attached to the quinoline ring, which exhibit characteristic stretching vibrations at 885, 741, and 698 cm^{-1}. In contrast, EFMPQC incorporates three C-F bonds, with corresponding stretching bands observed at 1087, 1010, and 991 cm^{-1}, which show excellent agreement with reported literature values [50, 51]. As discussed in the structural analysis, the C-Cl bond lengths are longer than the corresponding C-F bonds, reflecting the stronger bonding interaction in C-F bonds. This enhanced bond strength leads to higher force constants, causing the C-F stretching modes to appear at higher wavenumbers compared to the C-Cl stretching vibrations, which is consistent with fundamental principles of vibrational spectroscopy.

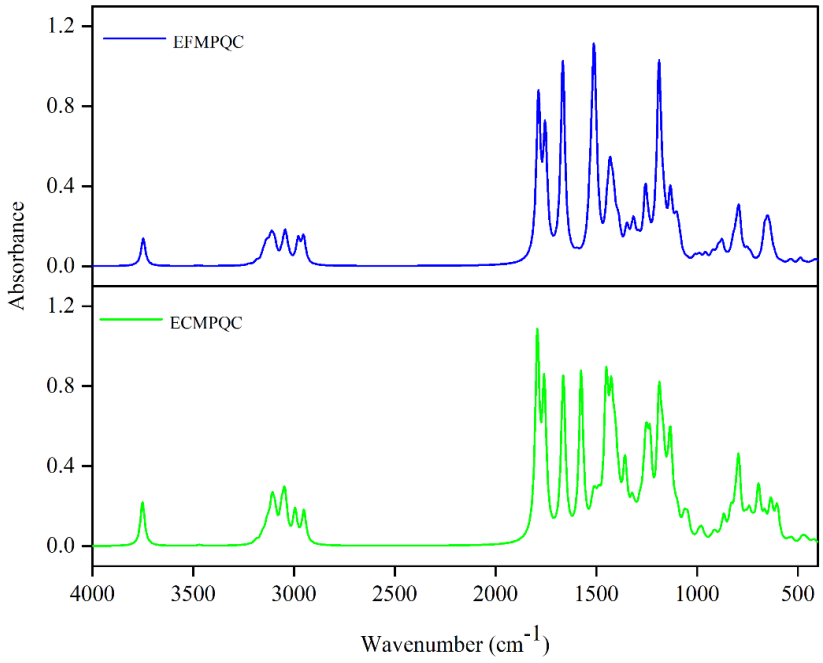

Figure 2. Simulated IR spectra of ECMPQC and EFMPQC

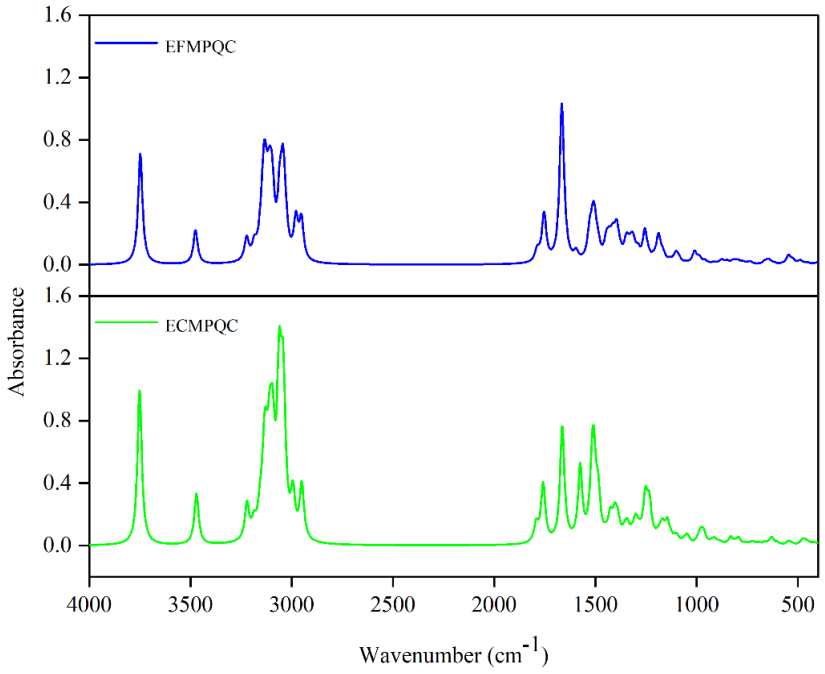

Figure 3. Simulated Raman spectra of ECMPQC and EFMPQC

Table 3. Simulated vibrational assignments of ECMPQC

Modes	Theoretical wavenumber			Vibrational assignments
	Unscaled	I_{IR}	I_{Raman}	
1	3751	78.90	263.43	υ OH (100)
2	3471	1.73	86.00	υ NH (100)
3	3221	0.60	61.95	υ CH (99)
4	3187	6.30	24.85	υ CH (94)
5	3157	13.01	38.73	υ CH (89)
6	3136	19.33	105.45	υ_{as} CH_3 (97)
7	3126	15.85	82.11	υ_{as} CH_3 (89)
8	3110	40.94	76.34	υ_{as} CH_3 (89)
9	3106	20.96	48.96	υ_{as} CH_2 (97)
10	3103	4.92	11.26	υ_{as} CH_2 (97)
11	3094	35.55	134.72	υ_{as} CH_2 (95)
12	3062	19.21	180.79	υ_{s} CH_3 (93)
13	3060	23.42	68.25	υ CH (89)
14	3047	49.56	52.75	υ_{s} CH_3 (89)
15	3044	19.45	113.76	υ_{s} CH_3 (78)
16	3038	14.71	93.43	υ_{s} CH_2 (98)
17	2994	56.41	72.34	υ_{s} CH_2 (93)
18	2950	57.82	92.63	υ_{s} CH_2 (97)
19	1792	357.46	30.62	υ CO (75)
20	1758	255.71	98.92	υ CO (82)
21	1663	292.71	197.41	υ CC (49), υ NC (14), δ HCC (14)
22	1575	295.18	124.41	υ CC (58)
23	1527	6.42	5.20	δ HCH (66)
24	1518	3.09	9.91	δ HCH (54), δ HNC (12)
25	1516	24.05	46.37	υ CC (32), δ HCH (20)
26	1512	10.72	28.49	δ HCH (41)
27	1511	1.67	41.87	δ HCH (45)
28	1507	3.35	27.68	δ HCH (78), τ HCCN (13)
29	1505	26.07	41.74	δ HCH (56)
30	1496	1.73	1.84	δ HCH (64)
31	1494	6.69	9.22	δ HCH (58)
32	1487	29.15	40.55	υ NC (11)
33	1484	7.05	23.98	δ HCH (34), δ HNC (26)
34	1450	247.47	6.06	υ NC (34)
35	1433	18.78	5.36	δ HCH (73)
36	1425	135.60	27.28	υ CC (17), υ OC (19), δ HCH (18), δ HOC (19)
37	1424	38.44	7.08	δ HCH (46)
38	1413	38.37	3.79	τ HCNC (44)
39	1406	57.43	10.68	υ NC (11), δ HCC (30)
40	1402	41.57	28.46	δ HCC (15), τ HCNC (38)
41	1389	29.65	23.93	δ HCC (26), τ HCNC (27)
42	1386	7.36	5.00	τ HCNC (42)
43	1373	7.58	0.87	δ HCC (24), δ HCN (25)
44	1357	114.44	12.79	υ CC (17), (10), δ HCC (20)
45	1342	10.43	25.25	τ HCNC (10)
46	1322	42.91	7.37	τ HCNC (31)
47	1308	14.45	8.55	δ HCN (32), τ HCNC (11)
48	1300	7.47	27.53	υ CC (11), δ HCC (21), τ HCNC (10)
49	1283	33.98	11.54	υ NC (10)
50	1265	33.15	5.11	υ CC (25)
51	1253	134.34	70.09	δ HOC (15)
52	1233	136.69	61.95	δ HCN (31)

53	1210	1.85	4.02	υ NC (41)
54	1188	199.74	8.40	υ OC (23), δ HOC (20)
55	1181	31.94	4.53	υ NC (12)
56	1170	94.96	24.03	υ NC (10)
57	1159	26.55	5.59	υ NC (22)
58	1144	31.63	31.05	δ CCC (14)
59	1132	146.92	4.24	υ CC (10)
60	1124	14.20	3.89	υ NC (25), δ HCN (11)
61	1106	20.14	5.08	υ CC (24), δ HCH (11), δ CCN (10), τ HCCN (40)
62	1096	26.62	8.89	υ CC (14)
63	1063	32.89	4.74	υ NC (11)
64	1046	35.83	14.14	δ HCN (11)
65	991	11.18	4.98	υ CC (10), (19), υ NC (19)
66	985	2.30	6.37	υ CC (38), δ HCC (11)
67	976	18.49	14.04	δ HCC (57)
68	964	1.79	15.71	δ CNC (14)
69	928	4.83	3.26	δ HCC (11)
70	914	12.93	6.51	υ CC (18), τ HCNC (13)
71	904	3.91	3.38	δ HCC (24)
72	885	2.49	3.56	υ ClC (14), (16), δ CNC (10)
73	867	40.71	1.00	τ HNCC (13)
74	832	44.80	12.20	υ NC (10)
75	809	31.61	2.63	τ OCCC (39), τ OCOC (24)
76	800	9.24	0.80	τ HCNC (29), τ HCCN (31)
77	793	123.17	7.81	υ NC (36), τ HNCC (25)
78	790	8.04	2.46	υ NC (13)
79	760	22.90	2.42	τ OCOC (35)
80	741	39.63	1.22	υ ClC (10), τ NCCC (14)
81	722	16.51	5.38	τ NCCC (28), τ HOCC (15)
82	698	50.63	1.16	υ ClC (29)
83	691	47.16	2.05	τ NCCC (30), τ HOCC (17)
84	664	33.80	3.83	τ NCCC (35), τ HOCC (13)
85	635	50.19	3.22	δ OCO (30)
86	628	20.37	9.97	τ CCCC (14), τ ClCCC (22), τ HOCC (24)
87	604	43.86	2.10	τ ClCCC (11), τ HOCC (40)
88	597	19.03	1.57	δ CCN (10)
89	546	4.12	6.40	δ CCN (22)
90	530	8.43	1.75	δ NCC (14)
91	481	6.80	1.85	τ CCNC (20)
92	475	4.43	5.97	δ NCC (10), τ CCNC (18)
93	464	8.72	4.68	δ NCC (22)
94	450	5.05	3.32	δ CNC (12), δ CCN (15), τ CNCC (11)
95	425	3.52	2.69	δ OCC (57)
96	414	5.62	1.22	δ CNC (16), τ ClCCC (13)
97	370	3.19	4.91	δ CCC (20), δ NCC (23)
98	366	1.07	4.78	τ ClCCC (11)
99	352	5.23	5.94	δ CNC (28)
100	344	3.91	0.80	δ CNC (20)
101	332	2.23	9.00	υ CC (11), δ CCN (16)
102	322	0.49	0.65	δ ClCC (24)
103	309	1.56	3.73	τ CCCC (22)
104	306	4.32	2.37	δ CCN (24)
105	298	2.68	5.09	δ ClCC (26), τ CCCC (22)
106	266	2.35	2.87	δ ClCC (21), τ CCCC (10)
107	254	1.89	1.51	δ NCC (10), τ CCCC (11)
108	243	0.34	2.28	δ ClCC (59)

109	240	0.48	0.60	τ HCCC (51)
110	233	0.27	1.55	δ ClCC (36)
111	212	1.11	0.71	δ ClCC (18)
112	204	1.02	0.73	δ ClCC (23), τ CCCC (14)
113	194	0.35	0.66	δ CCC (11), δ ClCC (24), δ NCC (15)
114	192	0.36	3.74	τ NCCC (10)
115	169	4.36	4.88	τ CNCC (10), τ NCCN (16)
116	147	0.40	0.67	δ CCC (23), δ NCC (16)
117	133	2.00	1.46	δ CCC (20), τ CCNC (15)
118	121	0.38	0.56	τ ClCCC (10), τ CCNC (26)
119	100	1.27	0.76	τ CCCC (20), τ CCCN (26)
120	81	0.11	1.58	τ CCCC (10), τ CNCC (43)
121	56	0.21	0.41	τ CCCC (13), τ CCNC (13)
122	50	0.25	1.78	τ CCCC (15), τ NCCC (15)
123	48	3.16	0.58	τ CCCN (11)
124	33	0.56	0.2	τ OCCC (81), τ CCNC (33)
125	25	0.35	1.19	τ CCCC (25), τ NCCC (20), τ CNCC (22)
126	23	1.36	1.10	τ CCCC (18), τ CCNC (27), τ CNCC (15)

υ - stretching, υs - symmetric stretching, υas - asymmetric stretching, τ- torsion, δ - deformation

Table 4. Simulated vibrational assignments of EFMPQC

Modes	Theoretical wavenumber			Vibrational assignments
	Unscaled	I_{IR}	I_{Raman}	
1	3748	71.9678	267.8615	υ OH (100)
2	3475	1.2728	82.2101	υ NH (100)
3	3223	2.1999	54.1922	υ CH (99)
4	3185	8.0492	33.9995	υ_{as} CH_2 (94)
5	3154	19.5977	43.3999	υ CH (76)
6	3138	18.8639	111.9508	υ_{as} CH_3 (96)
7	3138	13.5212	50.6178	υ CH (80)
8	3128	16.868	97.3806	υ_{as} CH_3 (97)
9	3114	42.4446	90.1355	υ_s CH_3 (90),
10	3106	5.3139	12.6061	υ_s CH_3 (94)
11	3104	15.6033	74.1153	υ_{as} CH_2 (87)
12	3095	36.7952	113.8191	υ CH (97)
13	3059	15.5035	129.6103	υ_s CH_3 (100)
14	3045	43.5839	95.3859	υ_s CH_2 (97)
15	3042	31.1291	99.6004	υ_s CH_3 (93)
16	3030	14.0454	55.5176	υ CH (88)
17	2979	59.5336	94.1157	υ_s CH_2 (94)
18	2952	66.5082	95.7159	υ_s CH_2 (97)
19	1787	406.8431	28.1167	υ CO (72)
20	1753	308.1074	117.0506	υ CO (76)
21	1666	510.8344	376.3861	υ CC (33), CC (14), NC (12)
22	1651	0.4717	19.2095	υ CC (58)
23	1595	7.618	20.3087	υ CC (49)
24	1532	36.7228	7.4876	δ HCH (75)
25	1528	67.7138	53.3481	υ CC (23), υ CN (10)
26	1517	3.8198	12.3547	δ HCH (59), δ HNC (10)
27	1514	81.3468	8.5478	δ HCH (49)
28	1512	306.5408	25.2102	δ HCH (62), τ HCCC (12)
29	1512	21.5869	14.6388	δ HCH (34)
30	1506	35.2364	19.6136	δ HCH (63)
31	1504	89.4746	49.6348	δ HCH (56)

32	1496	15.7234	4.1445	δ HCH (69)
33	1493	15.76	7.3534	δ HCH (72)
34	1486	8.6927	26.1794	δ HCH (14), δ HNC (28)
35	1446	75.3804	40.4087	υ NC (21)
36	1433	114.2075	31.0469	υ CC (30), υ CO (16), δ HOC (16)
37	1430	42.7649	5.0849	δ HCH (98)
38	1427	12.8542	1.3134	δ HCH (72)
39	1418	50.3009	18.3683	τ HCNC (33)
40	1415	58.1461	21.4299	δ HCC (16)
41	1407	17.9985	16.3049	δ HCC (13), τ HCNC (41)
42	1395	17.2734	64.7028	δ HCN (11)
43	1390	50.736	4.9736	δ HCC (16), τ HCNC (17)
44	1383	2.7495	6.1619	τ HCNC (15)
45	1377	4.3353	7.8639	δ HCN (27), δ HCC (24)
46	1349	63.7128	33.4336	υ CC (11), υ CF (11)
47	1340	5.8868	22.7511	υ CC (22), CC (14)
48	1324	20.327	26.4727	τ HCNC (26)
49	1315	55.0834	21.8766	δ HCN (15)
50	1311	19.7977	17.8528	δ HCN (10)
51	1290	31.4014	22.976	δ HCC (18), τ HCNC (10)
52	1256	164.0766	71.7147	δ HOC (17)
53	1240	30.7528	10.903	δ HCN (28), δ HCC (12)
54	1214	8.0126	5.917	υ CN (13)
55	1202	20.2918	3.4408	υ CN (16)
56	1191	66.1913	5.1201	υ CO (12)
57	1188	411.2749	57.8275	υ CO (18), δ HOC (21)
58	1168	59.755	15.7604	υ CN (10), υ CN (14), τ HCCC (10)
59	1158	24.5093	3.5968	τ HCCC (10)
60	1132	75.3976	1.7723	τ HCCC (22)
61	1131	73.5773	4.106	υ CN (10)
62	1111	23.3746	4.6035	υ CC (15), τ HCCN (37)
63	1100	67.5571	20.4657	υ CC (21), υ CN (15)
64	1087	36.697	9.3295	υ CC (12), υ CF (26), υ CN (15)
65	1051	2.8022	2.1133	δ HCN (14), υ CF (33)
66	1010	13.5498	28.0643	δ HCN (17)
67	991	10.3349	4.2768	υ CC (13), υ CF (28)
68	986	3.9254	7.5316	υ CC (38)
69	981	4.4477	2.6469	δ HCC (74), τ CCCN (13)
70	958	20.5677	6.7803	υ CC (14), δ HCC (10)
71	925	15.9367	0.4977	δ HCN (14)
72	916	11.3564	3.1764	δ HCC (12)
73	894	28.9949	1.0993	δ HCN (17)
74	875	46.7023	9.6893	τ HNCC (12)
75	850	5.1932	6.7812	υ CC (10), υ CN (19), δ CCC (10)
76	821	38.7826	6.2085	υ CN (10), τ HCCN (14)
77	806	5.758	4.6647	υ CN (11), τ HCCN (14)
78	804	37.0734	1.0204	τ OCOC (35), τ OCCC (41)
79	792	119.4277	5.6727	υ CN (16), τ HNCC (22)
80	771	5.2795	4.7374	δ FCC (12)
81	752	21.3692	1.4897	τ OCOC (43), τ OCCC (24)
82	736	17.4723	5.8122	δ OCC (20)
83	665	68.5782	4.8778	δ OCO (17)
84	650	17.4288	3.4389	τ NCCC (29), τ HOCC (13)
85	649	56.1342	5.1249	δ OCO (26), τ NCCC (10)
86	636	49.568	5.3565	τ HOCC (43)
87	617	13.0309	2.3599	τ NCCC (29), τ HOCC (20)

88	583	4.9195	0.5972	τ FCCC (31), τ CCCC (11), τ CCCC (17)
89	546	2.4839	19.5292	τ FCCC (22)
90	534	10.7882	2.7873	δ CCN (24)
91	524	1.3927	8.3378	δ CCC (10)
92	488	14.1403	8.1419	τ CCNC (14)
93	484	3.0743	0.7405	τ CCNC (19)
94	464	3.8859	1.2278	υ CC (10)
95	452	1.4486	2.7236	δ NCC (16)
96	432	4.9406	0.1988	δ CCN (14), δ OCC (26)
97	415	9.3898	1.2894	δ CNC (12), τ FCCC (14)
98	402	5.2627	0.8993	δ FCC (14)
99	396	0.3003	1.0818	δ OCC (17), δ CNC (15)
100	394	0.7379	0.6908	τ FCCC (17), τ FCCC (24)
101	378	4.0755	2.9117	δ CCC (14), δ OCC (11)
102	360	13.4206	13.9856	τ FCCC (22)
103	359	1.9225	2.1079	τ FCCC (18)
104	331	0.7473	1.4358	δ CCN (28), δ1 CNC (1)
105	319	1.2834	0.7776	δ FCC (61)
106	297	5.7833	0.4781	δ FCC (20)
107	281	0.5725	3.8431	δ FCC (16), δ CCN (10), δ NCC (10), δ CNC (12)
108	273	5.0306	2.8974	δ CNC (10)
109	254	1.1477	1.3692	τ HCCN (42)
110	238	0.4104	0.3528	τ CCCC (26)
111	228	0.0613	1.9023	τ HCCC (63)
112	211	0.2674	0.5673	τ HCCN (43)
113	205	0.7598	1.2674	τ HCCN (33)
114	200	0.4749	3.6335	δ NCC (16)
115	189	1.9706	3.1371	τ CNCC (13), τ CCNC (13)
116	158	1.1413	0.8356	τ NCCN (21)
117	149	0.4964	0.1901	δ CCC (25), δ NCC (19), τ CCNC (10)
118	141	0.8988	0.5438	δ CCC (15), τ CCCC (12), τ CCNC (19)
119	105	0.0515	0.6911	τ CCCC (19), τ CCNC (13), τ CCCN (15)
120	92	0.5021	0.4865	τ CCCC (11), τ CCCN (32)
121	62	0.9244	2.2884	τ CNCC (45)
122	57	1.4013	0.8307	δ CNC (10), τ CNCC (18), τ CCNC (36)
123	45	3.0561	0.5161	τ OCCC (83)
124	41	0.0337	0.534	τ CCCC (24), τ CCNC (10)
125	37	2.6085	0.9894	τ CCCC (22), τ CCNC (23), τ CCCN (12)
126	18	0.0153	0.4891	τ CNCC (32), τ CCCN (25)

υ - stretching, υs - symmetric stretching, υas - asymmetric stretching, τ- torsion, δ - deformation

The deformation modes of C-Cl groups in ECMPQC were calculated in the range of 322-194 cm^{-1}, whereas the C-F deformation modes in EFMPQC were observed between 402 and 281 cm^{-1}, showing good agreement with reported values [52, 53]. As discussed earlier, the shorter C-F bond length relative to C-Cl indicates stronger bonding, which results in vibrations occurring at higher frequencies. In addition, the deformation modes of CH_2 and CH_3 groups were calculated below 1500 cm^{-1} for both quinolone derivatives. The in-plane bending vibrations of methine (C-H) groups were observed between 1406 and 1300 cm^{-1} for ECMPQC, and 1415 and 1240 cm^{-1} for EFMPQC, whereas the out-of-plane bending modes were calculated in the ranges of 985-928 cm^{-1} for ECMPQC and 981-916 cm^{-1} for EFMPQC, respectively. These values show strong agreement with literature reports [54].

3.3. Electronic Properties

The key electronic characteristics of quinolone derivatives ECMPQC and EFMPQC, including oscillator strength (f), orbital contributions, and excitation energy (E), are summarized in Table. 5, and the corresponding computed UV-Vis spectra in the gas phase are illustrated in Figure 4.

In the present study, the quinolone derivative ECMPQC exhibits intense, moderate, and weak absorption bands at 341, 363, and 359 nm, corresponding to excitation energies of 3.633, 3.412, and 3.452 eV, respectively.

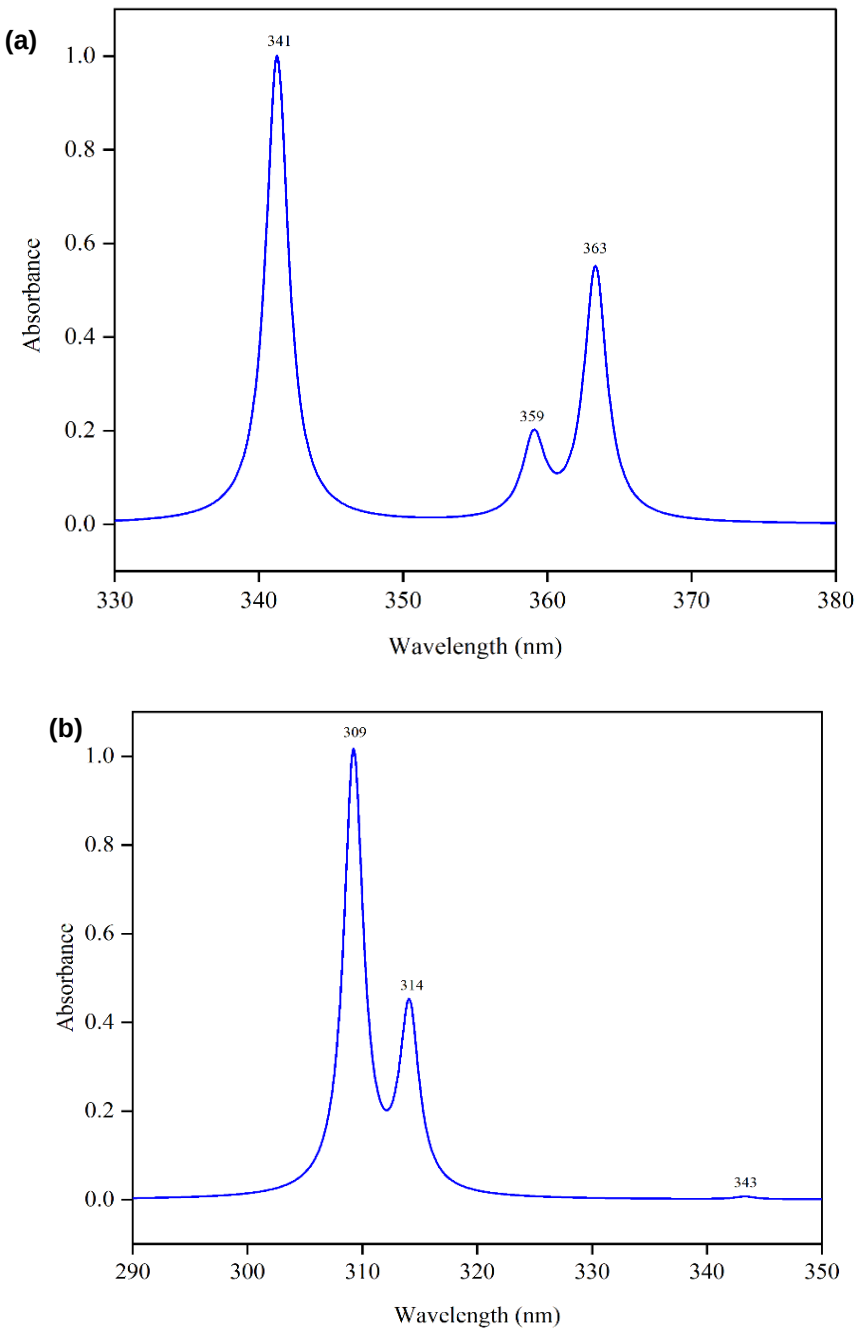

Figure 4(a). Calculated electronic spectrum of ECMPQC, **(b)** EFMPQC

Table 5. Calculated wavelengths (λ), excitation energies (E), and oscillator strengths (f), and contributions (major and minor) of quinolone derivative in the gas phase

Derivatives	λ (nm)	E (eV)	f	Major contributions	Minor contributions
ECMPQC	363	3.412	0.025	H-2→L (29%), H→L (61%)	H-2→L+1 (3%), H-1→L (3%)
	359	3.452	0.008	H-2→L (47%), H→L (32%)	H-2→L+1 (5%), H-1→L (6%)
	341	3.633	0.0461	H→L+1 (85%)	H-1→L (6%), H-2→L (4%), H→L (2%)
EFMPQC	343	3.611	0.0001	H-2→L (82%), H-2→L+1 (13%)	H-2→L+3 (3%)
	314	3.947	0.0069	H→L (77%)	H→L+1 (5%)
	309	4.009	0.0168	H-2→L+1 (66%), H-2→L (14%), H→L+1 (13%),	H-1→L (2%), H→L (4%)

Table 6. The FMO energies and energy gap of quinolone derivatives in the gas phase

Parameters	Formula	ECMPQC	EFMPQC
E_{HOMO} (eV)	-	-5.7889	-5.8803
E_{LUMO} (eV)	-	-1.7529	-1.3622
$E_{HOMO-LUMO}$ gap(eV)	-	4.0360	4.5181
Ionization potential (I)	$-E_{HOMO}$	5.7889	5.8803
Electron affinity (A)	$-E_{LUMO}$	1.7529	1.3622
Electronegativity (χ)	(I+A)/2	3.7709	3.6212
Chemical potential (μ)	-χ	-3.7709	-3.6212
Chemical hardness (η)	(I-A)/2	2.0180	2.2590
Chemical softness (s)	1/2η	0.2477	0.2213
Global Electrophilicity (ω)	$\mu^2/2\eta$	3.5232	2.9024
Maximum electron charge (ΔNmax)	−(μ/η)	1.8686	1.6030

(a)

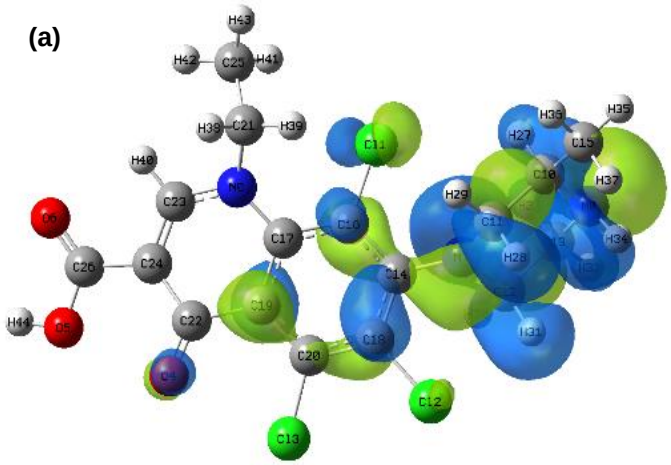

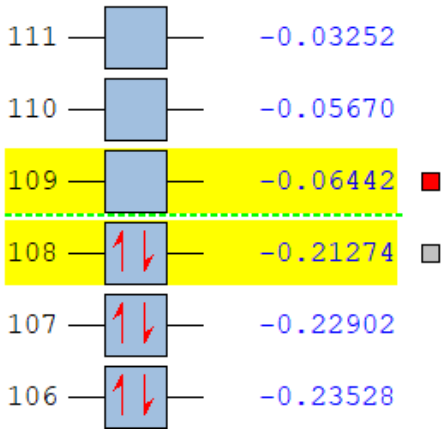

E_{HOMO}= -5.7889 eV

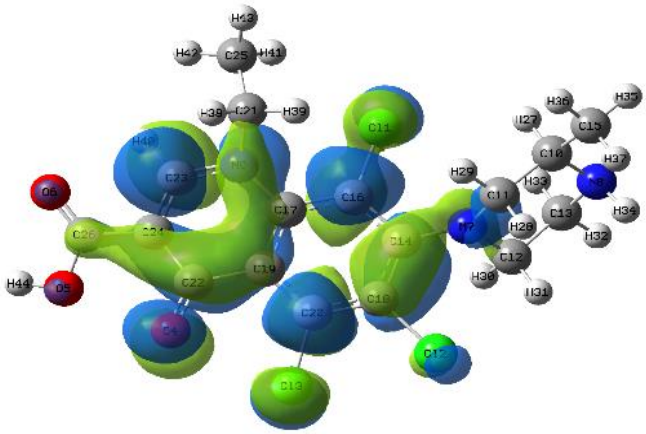

***E_{LUMO}*= -1.7529 eV**

Figure 5(a). Calculated HOMO-LUMO energy gap of ECMPQC

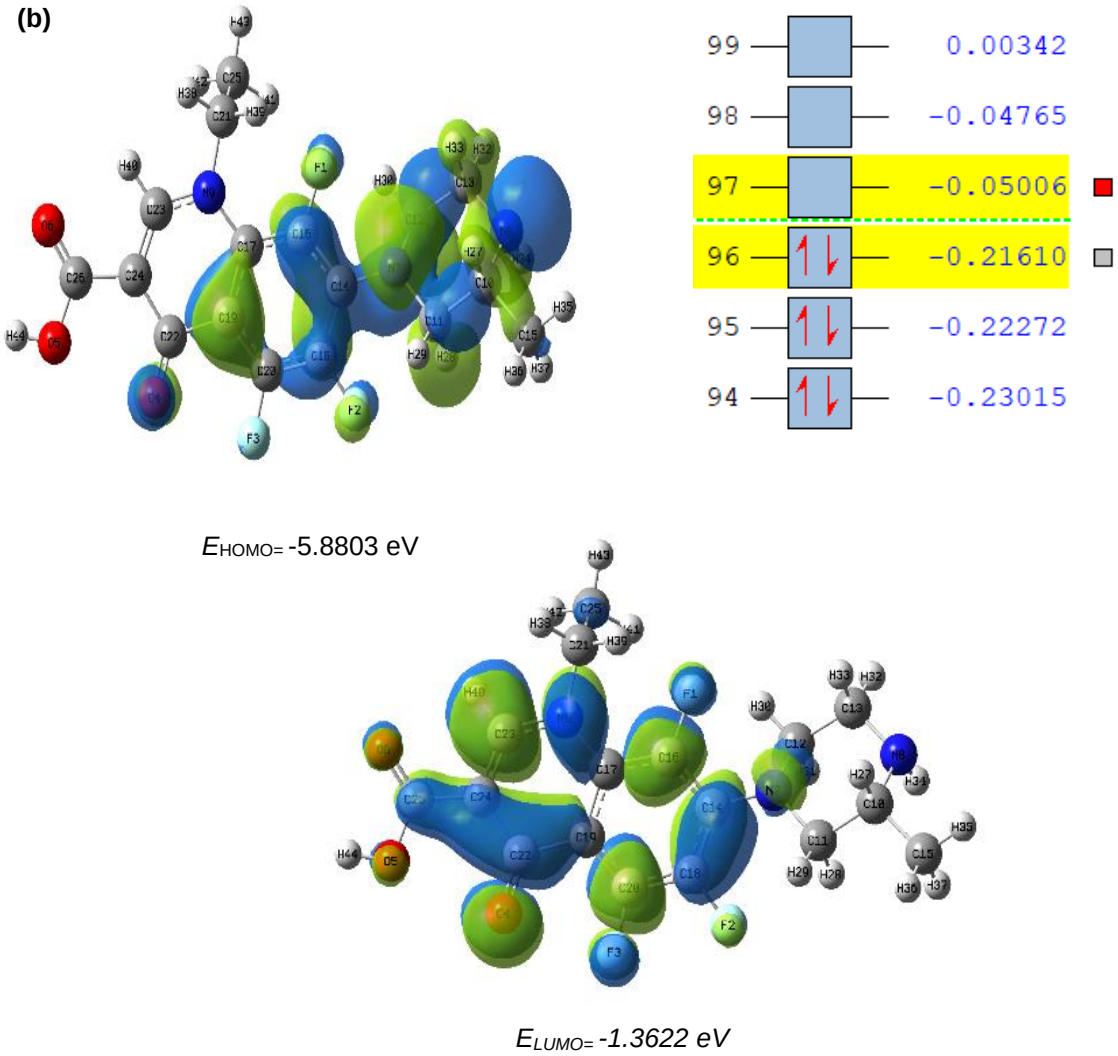

Figure 5(b). Calculated HOMO-LUMO energy gap of EFMPQC

The most intense absorption band, calculated at 341 nm, originates primarily from the HOMO → LUMO (H → L) electronic transition, with a contribution of 61%. In contrast, the quinolone derivative EFMPQC shows intense, moderate, and weak absorption peaks at 309, 314, and 343 nm, with corresponding excitation energies of 4.009, 3.947, and 3.611 eV, respectively. The dominant absorption band, simulated at 309 nm, arises mainly from the HOMO−2 → LUMO (H−2 → L) transition, contributing 82% to the excitation. A bathochromic (red) shift is observed for the chlorinated derivative ECMPQC, which can be attributed to enhanced electron cloud delocalization and increased polarizability of chlorine atoms, resulting in a reduced HOMO–LUMO energy gap of 4.036 eV. In contrast, the fluorinated derivative EFMPQC exhibits a hypsochromic (blue) shift, arising from the lower polarizability and strong inductive electron-withdrawing nature of fluorine, leading to an increased energy gap of 4.5181 eV. These findings indicate that the chlorinated derivative possesses higher chemical reactivity but lower kinetic stability, whereas the fluorinated derivative demonstrates reduced reactivity and enhanced stability. The frontier molecular orbital (FMO) distributions of ECMPQC and EFMPQC are graphically illustrated in Fig. 5, and the corresponding numerical energy values are presented in Table 6. In the FMO plots, the positive and negative phases of the molecular orbitals are visually represented using yellow and blue color codes for the LUMO and HOMO, respectively. In addition, the density of states (DOS) spectra of the quinolone derivatives is depicted in Fig. S1 (Supplementary Material).

3.4. NBO Analysis

Natural bond orbital (NBO) analysis was employed to elucidate the intramolecular charge-transfer interactions within the optimized structures of the quinolone derivatives ECMPQC and EFMPQC. The computed NBO parameters for both systems are summarized in Tables 7 and 8, respectively. The analysis reveals a significant donor–acceptor interaction arising from the electron donation from the lone pair

orbital of O5 to the antibonding orbital of O6–C26 within the carboxylic acid (COOH) group of ECMPQC, resulting in a stabilization energy of 50.53 kJ/mol through an LP(2) → π* transition. In EFMPQC, the dominant stabilization contribution originates from electron donation from C19 in the quinoline ring to the antibonding N9–C17 orbital, with a high stabilization energy of 302.62 kJ/mol, corresponding to an LP(1) → π* transition. The second major stabilization interaction in ECMPQC arises from electron donation from the lone pair on N9 to the antibonding orbitals of C23–C24, with a stabilization energy of 41.16 kJ/mol, also via an LP(1) → π* transition. In contrast, the EFMPQC system exhibits its second significant contribution from electron donation from C19 to the antibonding orbitals of C18–C20, yielding a stabilization energy of 84.06 kJ/mol. In the ECMPQC system, moderate stabilization energies were observed for interactions involving lone pair electrons on Cl2 and Cl3 donating into the antibonding π* orbital of the C18–C20 bond, with second-order perturbation energies of 13.15 and 15.81 kJ/mol, respectively, corresponding to LP(3) → π* delocalizations.

Table 7. Second-order perturbation theory of Fock matrix in selected NBO basis for ECMPQC

	Donor (i)	Type	Acceptor (j)	Type	Transition	E(2)[a] (KJ/mol)	E(j)-E(i)[b] (a.u)	F(i,j)[c] (a.u)
1	C_{14}-C_{16}	π	C_{17}-C_{19}	π*	π- π*	20.22	0.29	0.071
2	C_{14}-C_{16}	π	C_{18}-C_{20}	π*	π- π*	15.03	0.27	0.059
3	C_{17}-C_{19}	π	O_4-C_{22}	π*	π- π*	16.25	0.31	0.065
4	C_{17}-C_{19}	π	C_{14}-C_{16}	π*	π- π*	17.15	0.27	0.061
5	C_{17}-C_{19}	π	C_{18}-C_{20}	π*	π- π*	22.20	0.26	0.069
6	C_{18}-C_{20}	π	C_{14}-C_{16}	π*	π- π*	20.25	0.29	0.071
7	C_{18}-C_{20}	π	C_{17}-C_{19}	π*	π- π*	14.89	0.30	0.062
8	C_{23}-C_{24}	π	O_4-C_{22}	π*	π- π*	23.57	0.31	0.077
9	C_{23}-C_{24}	π	O_6-C_{26}	π*	π- π*	22.30	0.30	0.074
10	Cl_1	LP(3)	C_{14}-C_{16}	π*	LP(3)- π*	10.74	0.33	0.058
11	Cl_2	LP(3)	C_{18}-C_{20}	π*	LP(3)- π*	13.15	0.31	0.063
12	Cl_3	LP(3)	C_{18}-C_{20}	π*	LP(3)- π*	15.81	0.29	0.067
13	O_4	LP(2)	C_{19}-C_{22}	π*	LP(2)- π*	23.68	0.65	0.112
14	O_4	LP(2)	C_{22}-C_{24}	π*	LP(2)- π*	20.02	0.71	0.108
15	O_5	LP(2)	O_6-C_{26}	π*	LP(2)- π*	50.53	0.33	0.118
16	O_6	LP(2)	O_5-C_{26}	σ*	LP(2)- σ*	31.18	0.63	0.127
17	O_6	LP(2)	C_{24}-C_{26}	σ*	LP(2)- σ*	19.02	0.69	0.104
18	N_7	LP(1)	C_{14}-C_{16}	π*	LP(1)- π*	11.94	0.24	0.050
19	N_9	LP(1)	C_{17}-C_{19}	π*	LP(1)- π*	26.83	0.28	0.079
20	N_9	LP(1)	C_{23}-C_{24}	π*	LP(1)- π*	41.16	0.31	0.104

Table 8. Second-order perturbation theory of Fock matrix in selected NBO basis for EFMPQC

	Donor (i)	Type	Acceptor (j)	Type	Transition	E(2)[a] (KJ/mol)	E(j)-E(i)[b] (a.u)	F(i,j)[c] (a.u)
1	N_9-C_{17}	π	C_{23}-C_{24}	π*	π- π*	28.90	0.37	0.094
2	C_{14}-C_{16}	π	N_9-C_{17}	π*	π- π*	33.95	0.22	0.091
3	C_{14}-C_{16}	π	C_{18}-C_{20}	π*	π- π*	16.88	0.29	0.064
5	C_{18}-C_{20}	π	C_{14}-C_{16}	π*	π- π*	21.83	0.29	0.073
6	C_{23}-C_{24}	π	O_4-C_{22}	π*	π- π*	23.82	0.31	0.078
7	C_{23}-C_{24}	π	O_6-C_{26}	π*	π- π*	22.93	0.30	0.075
8	F_1	LP(3)	C_{14}-C_{16}	π*	LP(1)- π*	15.09	0.43	0.080
9	F_2	LP(3)	C_{18}-C_{20}	π*	LP(3)- π*	17.30	0.42	0.083
10	F_3	LP(3)	C_{18}-C_{20}	π*	LP(3)- π*	21.65	0.41	0.091
11	O_4	LP(2)	C_{19}-C_{22}	σ*	LP(2)- σ*	22.43	0.65	0.109
12	O_4	LP(2)	C_{22}-C_{24}	σ*	LP(2)- σ*	19.19	0.70	0.105
13	O_5	LP(2)	O_6-C_{25}	π*	LP(2)- π*	48.09	0.33	0.115
14	O_6	LP(2)	O_5-C_{26}	σ*	LP(2)- σ*	29.12	0.63	0.123
15	O_6	LP(2)	C_{24}-C_{26}	σ*	LP(2)- σ*	17.77	0.68	0.101
16	N_7	LP(1)	C_{14}-C_{16}	π*	LP(1)- π*	18.45	0.26	0.066
17	C_{19}	LP(1)	O_4-C_{22}	π *	LP(1)- π*	50.03	0.17	0.099
18	C_{19}	LP(1)	N_9-C_{17}	π*	LP(1)- π*	302.62	0.06	0.125
19	C_{19}	LP(1)	C_{18}-C_{20}	π*	LP(1)- π*	84.06	0.13	0.108

By comparison, the fluorinated derivative EFMPQC exhibits higher stabilization energies for analogous interactions involving lone pairs on F2 and F3, with values of 17.30 and 21.65 kJ/mol, respectively. The enhanced stabilization observed in the fluorine-substituted system can be attributed to the higher electronegativity and stronger orbital overlap of fluorine, which facilitates more effective electron delocalization into π* orbitals, thereby resulting in stronger donor–acceptor interactions compared to the chlorine-substituted analogue.

3.5. MEP analysis

The molecular electrostatic potential (MEP) surface maps of the quinolone derivatives ECMPQC and EFMPQC are presented in Fig. S2 (Supplementary Material), with electrostatic potential values ranging from -7.121×10^{-2} to 7.121×10^{-2} e.s.u. for ECMPQC and -7.843×10^{-2} to 7.843×10^{-2} e.s.u. for EFMPQC, respectively. The color-coded surface representations indicate electron-rich (red), electron-poor (blue), and electrostatically neutral (green) regions. In both quinolone derivatives, the red regions localized around the oxygen atoms O6 of the carboxylic acid (COOH) group and O4 of the keto (C=O) group indicate areas of high electron density and negative electrostatic potential, identifying these sites as potential nucleophilic centres. Conversely, the blue regions surrounding the hydrogen atoms of the hydroxyl (O–H), methylene (CH_2), and methyl (CH_3) groups, particularly at the periphery of the quinolone and piperazine rings, correspond to electron-deficient zones with positive electrostatic potential, suggesting their susceptibility to electrophilic attack. Additionally, the green regions distributed over the quinoline and piperazine ring systems reflect areas of near-neutral electrostatic potential, indicating electronically balanced regions within the molecular framework.

3.6. Topological parameters

3.6.1. ELF and LOL

Electron localization function (ELF) and localized orbital locator (LOL) analyses provide valuable insights into bonding characteristics and charge distribution within the molecular frameworks of chemical systems [55]. The contour maps, color-filled plots, and projection graphs for ELF and LOL analyses are illustrated in Figures. 6-9.

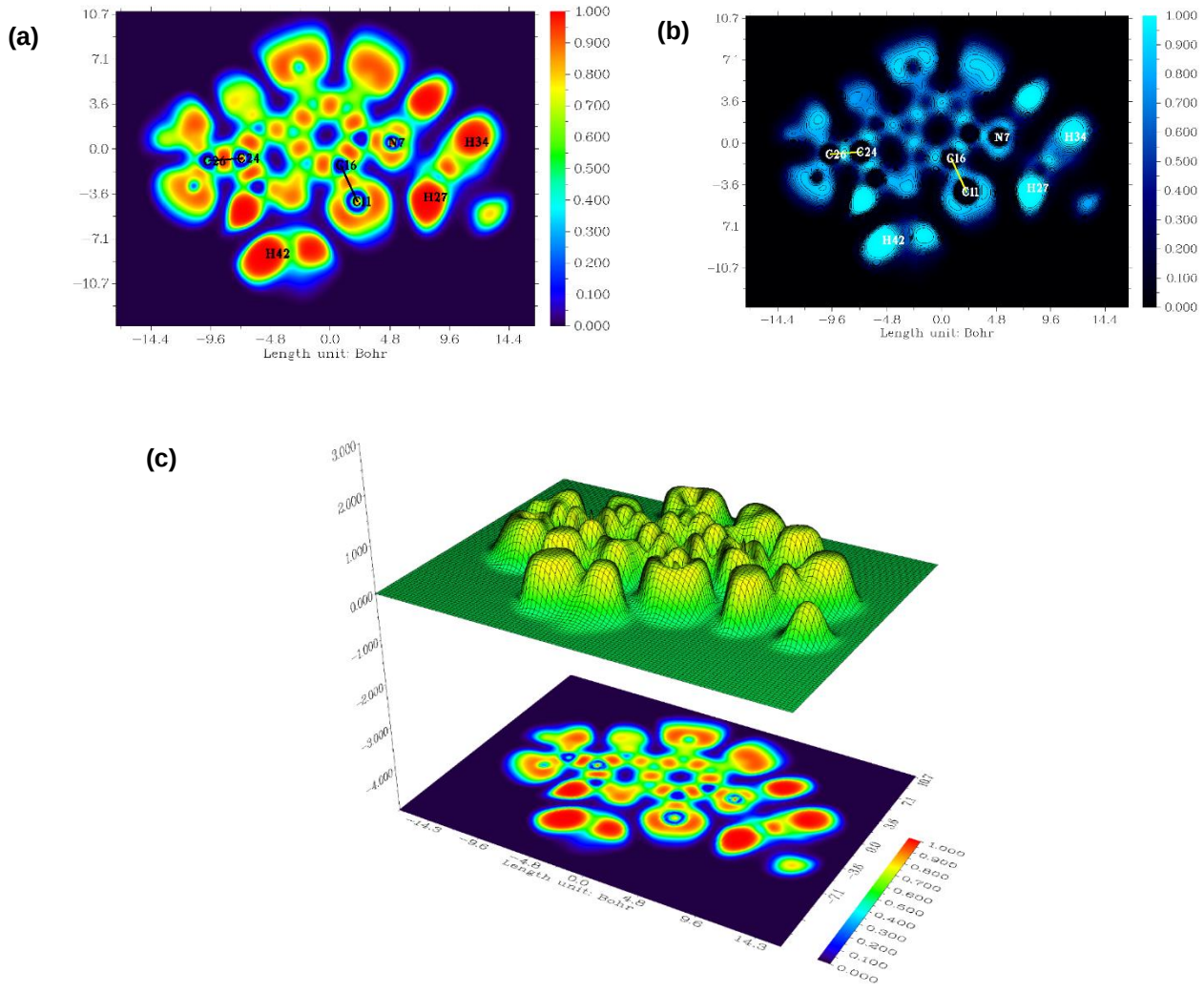

Figure 6 (a) ELF color map with numbering, **(b)** contour map, and **(c)** ELF color map with projection of ECMPQC

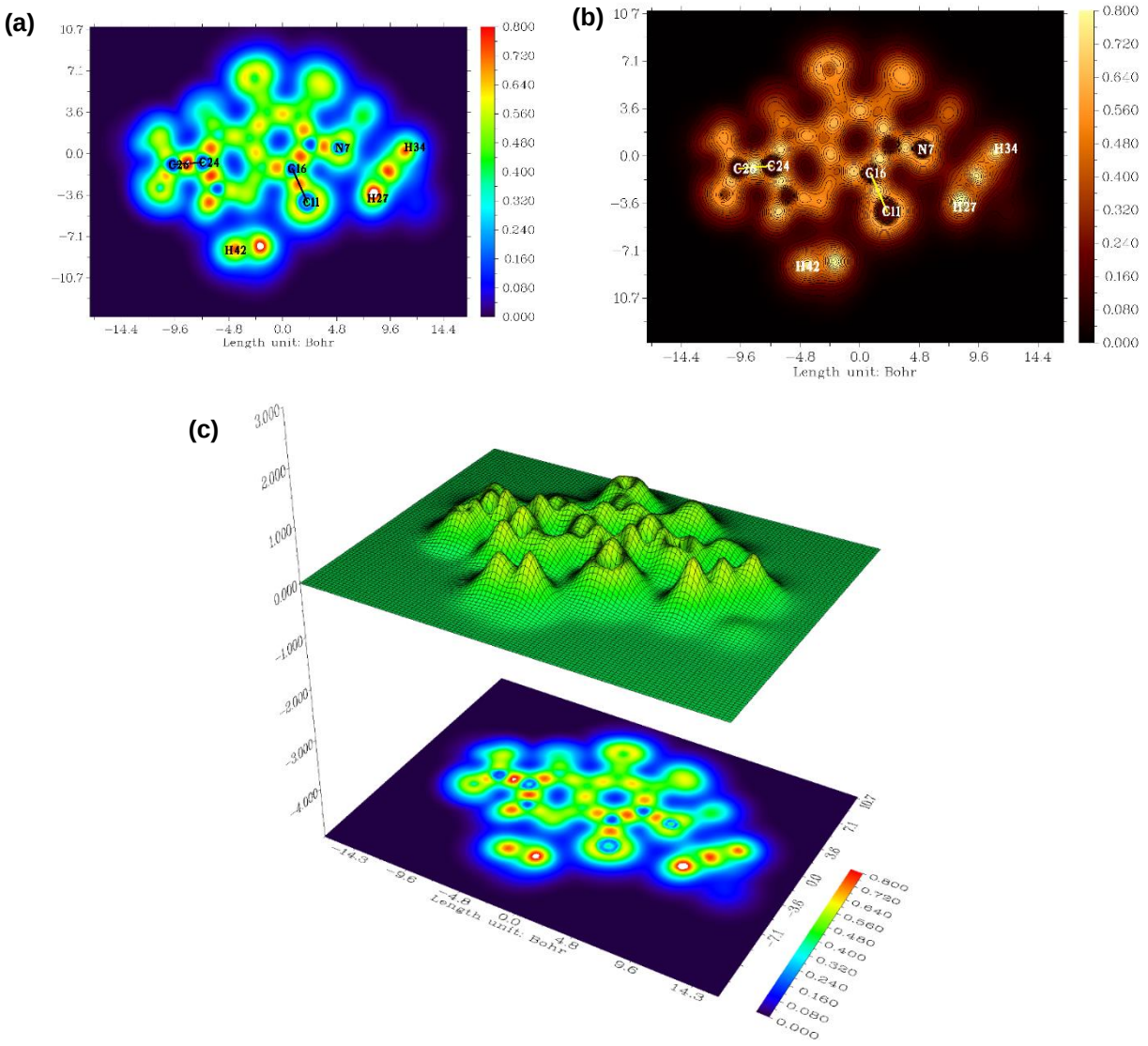

Figure 7(a) LOL color map with numbering, **(b)** contour map, and **(c)** ELF color map with projection of ECMPQC

In ECMPQC, the red regions localized around hydrogen atoms H34 and H27 in the piperazine ring, as well as H42 in the ethyl group attached to N9 of the quinolone ring, indicate highly localized electron density. In contrast, the blue regions surrounding carbon atoms C24 and C16 and chlorine atom Cl1 in the quinoline ring, C26 in the carboxyl group, and N7 in the piperazine ring, represent electron-delocalized regions within the molecular framework. Similarly, in EFMPQC, the red-colored regions around hydrogen atom H44 in the carboxyl group, H40 bonded to carbon C23 at the ortho position relative to the carboxyl (COOH) group, and hydrogen atoms H33 and H37 in the piperazine ring, emphasize localized electron density. Conversely, the blue regions distributed around atoms C26, O5, and O6 in the carboxyl group, as well as C24, C23, N9, C21, C17, C16, and F1 in the quinoline ring, indicate electron delocalization. These observations are consistent with the LOL analysis, further confirming the distribution of localized and delocalized electrons in both ECMPQC and EFMPQC.

3.6.2. RDG and NCI

Reduced density gradient (RDG) and noncovalent interaction (NCI) analyses were employed to identify and visualize intra- and intermolecular noncovalent interactions within the molecular structures of the quinolone derivatives [56]. The two-dimensional RDG scatter plots and three-dimensional NCI isosurface maps are shown in Figs. 10 and 11, respectively. In the RDG scatter plots, the regions characterized by electron density ($\rho \approx 0$) and the second eigenvalue of the Hessian matrix ($\lambda_2 \approx 0$) correspond to van der Waals interactions. Regions exhibiting higher electron density with negative λ_2 values ($\rho > 0$, $\lambda_2 < 0$) indicate the presence of attractive interactions such as hydrogen bonding, whereas regions with positive λ_2 values ($\rho > 0$, $\lambda_2 > 0$) are associated with steric repulsion.

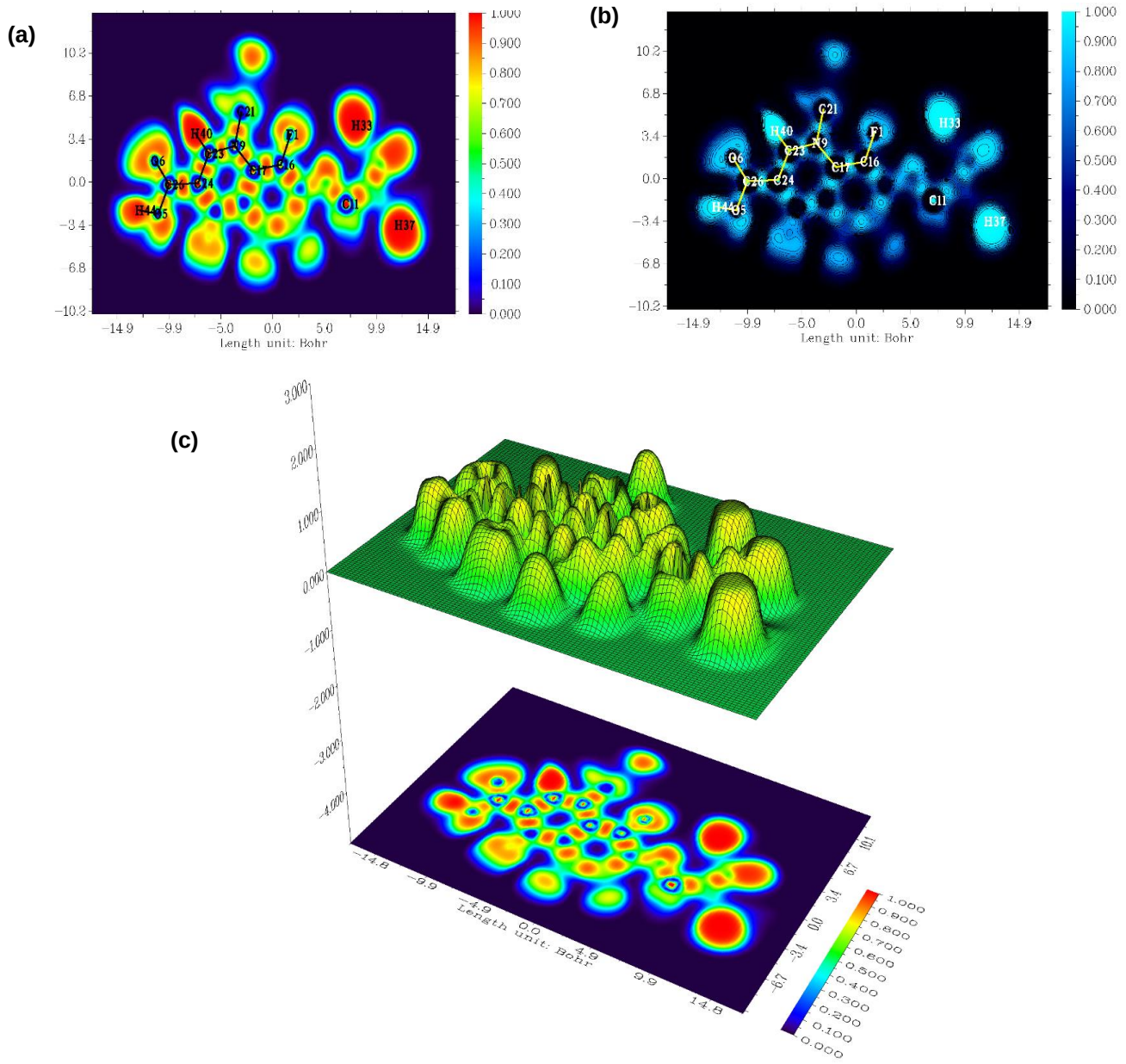

Figure 8(a) ELF color map with numbering, (b) contour map, and (c) ELF color map with projection of EFMPQC

In the present study, pronounced green and red features were observed in the RDG plots of both ECMPQC and EFMPQC, indicating that the molecular frameworks are stabilized primarily by van der Waals interactions and steric effects. The corresponding NCI isosurface maps show red-colored regions embedded within the quinoline and piperazine rings, reflecting steric repulsions, while green patches located at the interfaces of methyl (CH_3), carboxyl (COOH), and methylene (CH_2) groups signify the presence of weak van der Waals interactions that contribute to the overall molecular stability.

3.7. Molecular docking

Molecular docking analysis was performed to predict ligand–protein interactions by evaluating the formation of polar and nonpolar contacts within the active binding pockets, thereby creating a favorable environment for catalytic inhibition [57, 58]. In the present study, the binding affinities of the quinolone derivatives ECMPQC and EFMPQC were investigated against the SARS-CoV-2 main protease (Mpro) and RNA-dependent RNA polymerase (RdRp) enzymes. The three-dimensional crystal structures of SARS-CoV-2 Mpro (PDB ID: 6LU7) and RdRp (PDB ID: 7BV2) were retrieved from the Protein Data Bank (PDB), with resolutions of 2.50 Å and 2.16 Å, respectively. Co-crystallized ligands and water molecules were removed, and the proteins were prepared and saved in PDB format. The optimized molecular structures of ECMPQC and EFMPQC were converted to PDBQT format for docking simulations.

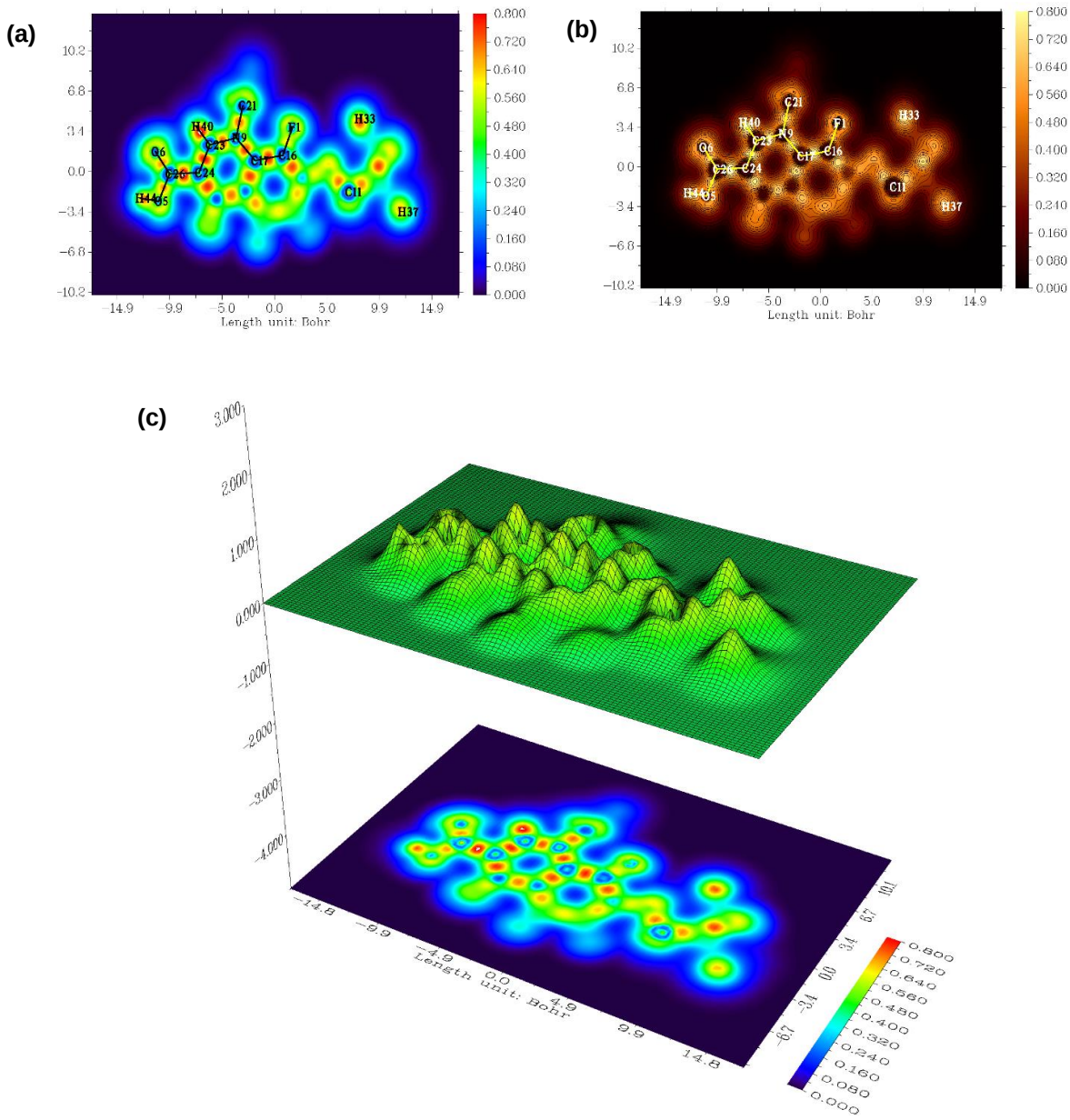

Figure 9(a). LOL color map with numbering, **(b)** contour map, and **(c)** ELF color map with projection of EFMPQC

The ligands ECMPQC and EFMPQC exhibited binding affinities of −5.14 and −4.89 kcal/mol, respectively, toward the 6LU7 (Mpro) protein, and −6.06 and −4.93 kcal/mol, respectively, toward the 7BV2 (RdRp) protein. For the Mpro (6LU7) enzyme, ECMPQC forms three hydrogen bonds with the amino acid residues Ala285, Thr199, and Met276. These interactions involve the oxygen atoms of the carboxyl group and the nitrogen atoms of the piperazine ring, with bond distances of 3.15 Å, 2.82 Å, and 2.86 Å, respectively. Similarly, EFMPQC forms three hydrogen bonds with the amino acid residues Thr190, His41, and Cys145, involving the carboxyl oxygen and piperazine nitrogen atoms, with bond lengths of 3.05 Å, 2.94 Å, and 3.29 Å, respectively, within the active site of the main protease. Previous studies report that standard antiviral drugs, such as lopinavir, darunavir, and amprenavir, exhibit stronger binding affinities of −9.91, −8.84, and −8.65 kcal/mol, respectively.

Although the quinolone derivatives show comparatively moderate binding energies, they interact directly with key catalytic residues of the enzyme, suggesting their potential inhibitory relevance [59]. For the RdRp (7BV2) enzyme, ECMPQC and EFMPQC form one and two hydrogen bonds, respectively, with active-site amino acid residues Lys621 and Lys890 (ECMPQC) and Lys426 (EFMPQC). The two-dimensional (2D) and three-dimensional (3D) ligand–protein interaction maps are illustrated in Figs. 12 and 13, and the corresponding binding energies, hydrogen bonding, and hydrophobic interactions are summarized in Table 9. According to literature, the co-crystallized antiviral drug remdesivir exhibits a binding affinity of −7.8 kcal/mol toward RdRp.

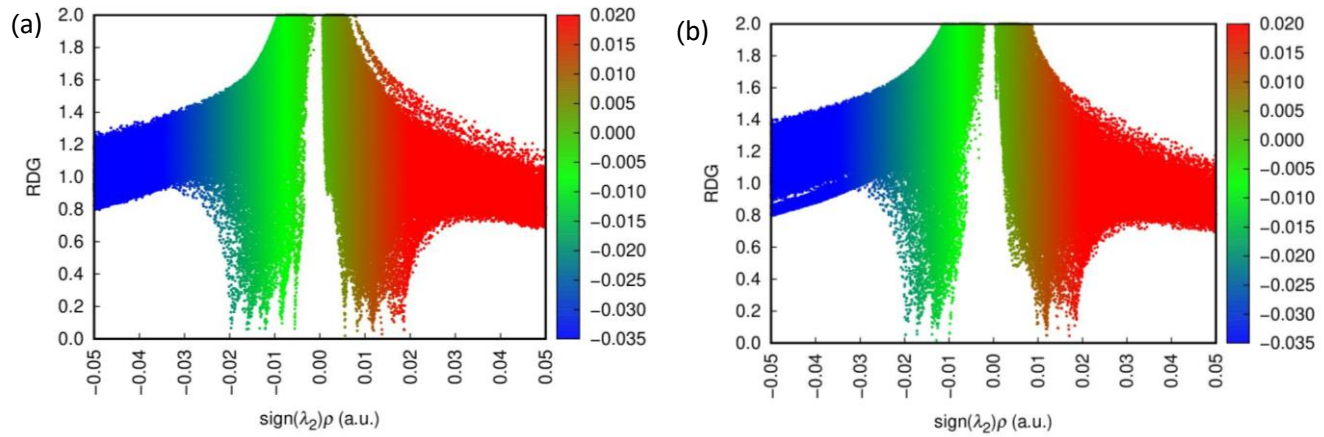

Figure 10(a). RDG scatter graph of **(a)** ECMPQC and **(b)** EFMPQC

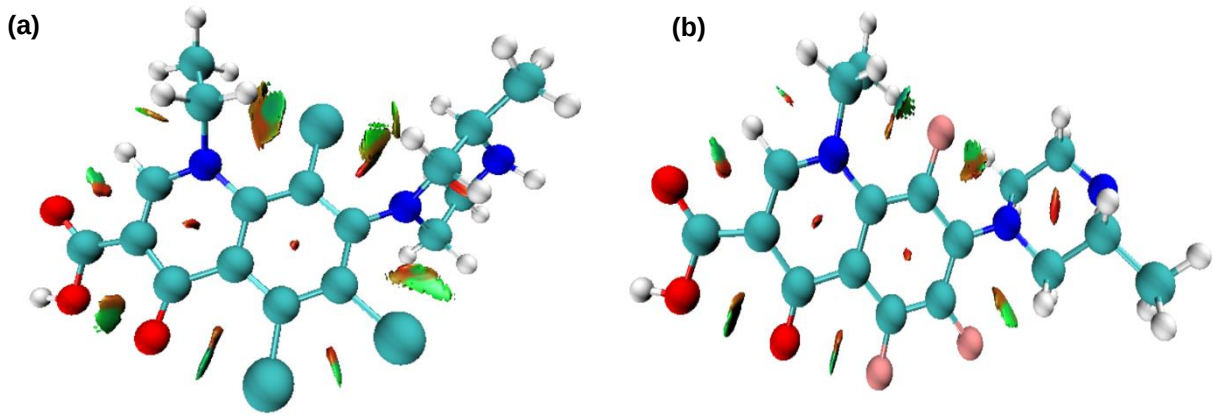

Figure 11(a) NCI isosurface graph of **(a)** ECMPQC and **(b)** EFMPQC

Table 9. Molecular docking of quinolone derivatives against 6LU7 and 7BV2 proteins

Ligands	PDB.IDs	Binding energy	Polar interactions	Bond distances (Å)	Hydrophobic interactions
ECMPQC	6LU7	-5.14	Alanine 285 Threonine 199 Methionine 276	3.15 2.82 2.86	Leucine 286, 287, 271 Tyrosine 237, 239 Glycine 275
	7BV2	-6.06	Lysine 621	2.59	Lysine 798 Tyrosine 619 Proline 620 Asparagine 618, 761, 760 Glutamic acid 811 Arginine 553
EFMPQC	6LU7	-4.89	Threonine 190 Histidine 41 Cysteine 145	3.05 2.94 3.29	Methionine 165 Arginine 188 Glutamine 189, 192 Proline 168 Leucine 167 Glutamic acid 166 Histidine 164
	7BV2	-4.93	Lysine 890 Lysine 426	2.93 2.89	Asparagine 893 Arginine 889 Phenylalanine 422

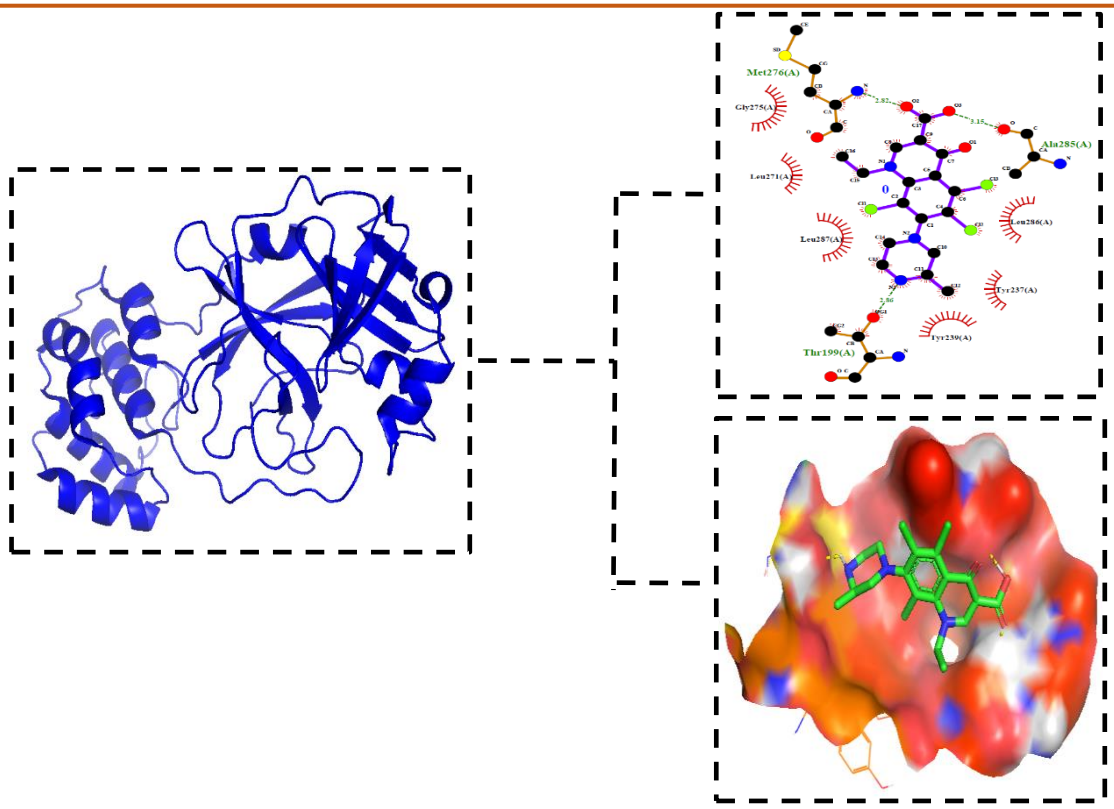

Figure 12(a). The 3D PyMOL and 2D LigPlot+ view of ECMPQC with 6LU7

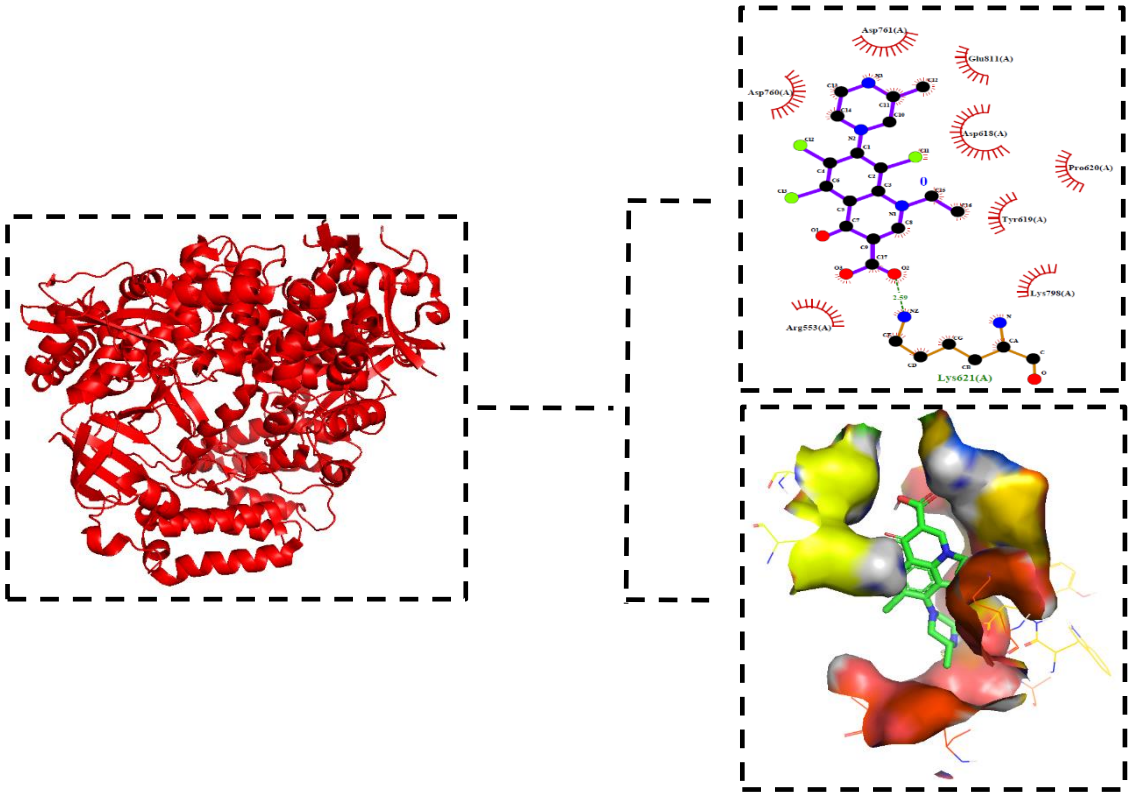

Figure 12(b). The 3D PyMOL and 2D LigPlot+ view of ECMPQC with 7BV2

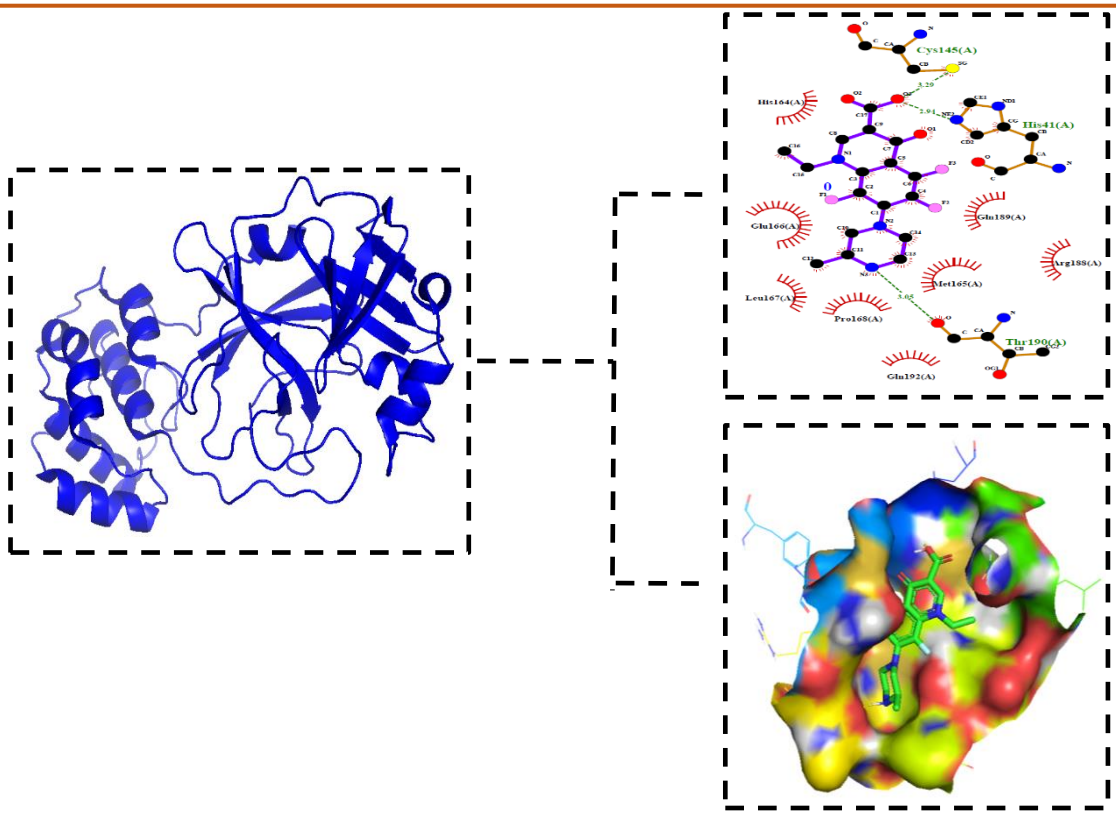

Figure 13(a). The 3D PyMOL and 2D LigPlot+ view of EFMPQC with 6LU7

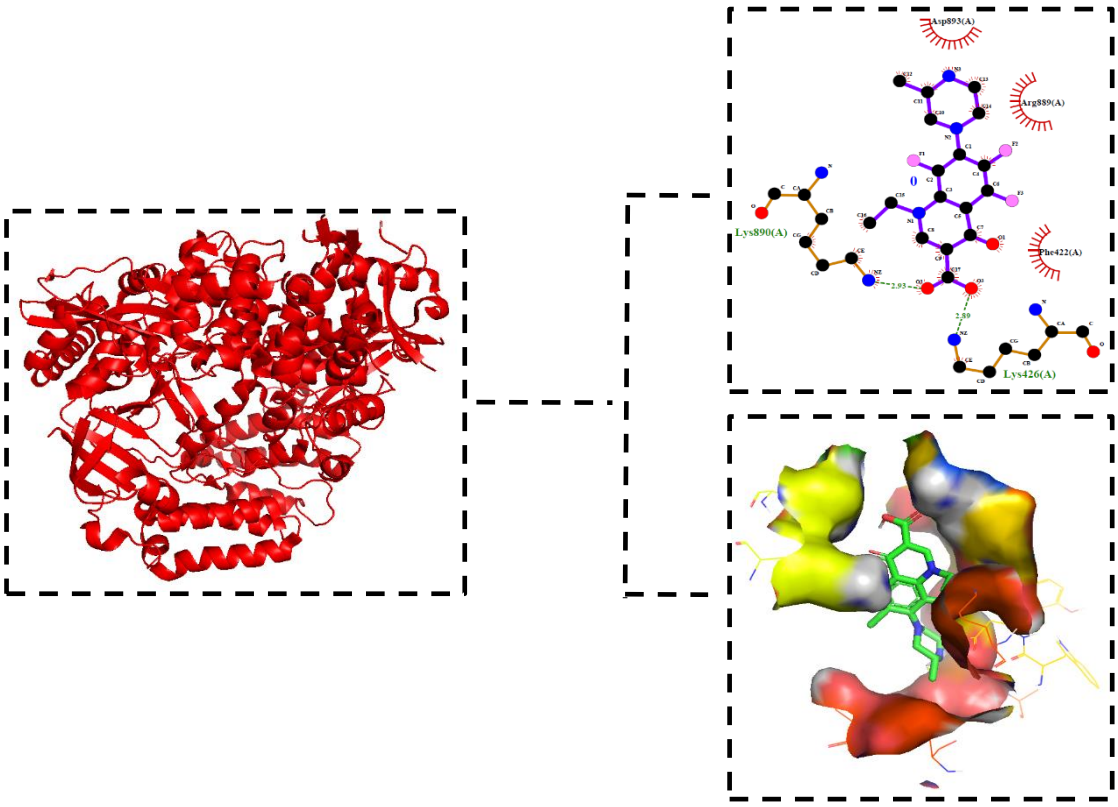

Figure 13(b). The 3D PyMOL and 2D LigPlot⁺ view of EFMPQC with 7BV2

In comparison, the quinolone derivatives show binding energies of −6.06 kcal/mol (ECMPQC) and −4.93 kcal/mol (EFMPQC). Notably, the chlorinated derivative ECMPQC demonstrates stronger binding interactions with key active-site residues than the fluorinated analogue [60]. The enhanced binding affinity of ECMPQC can be attributed to the larger atomic size, higher polarizability, and increased hydrophobic

character of chlorine, which collectively strengthen ligand–protein interactions.

4. Conclusion

The quinolone derivatives ECMPQC and EFMPQC were comprehensively characterized in terms of their structural, spectroscopic, electronic, and biological properties. The fluorinated derivative EFMPQC exhibits enhanced conformational stability, which is attributed to the shorter and stronger C–F bonds compared to the longer C–Cl bonds in ECMPQC. In the vibrational analysis, the C–F stretching modes appear at higher wavenumbers than the corresponding C–Cl vibrations, confirming the theoretical expectation that stronger chemical bonds vibrate at higher frequencies. From the electronic property analysis, the larger HOMO–LUMO energy gap and hypsochromic shift observed for EFMPQC indicate lower chemical reactivity and greater stability, which arise from the strong inductive electron-withdrawing effect and low polarizability of fluorine. In contrast, ECMPQC exhibits a bathochromic shift, reduced energy gap, and enhanced electron delocalization, suggesting higher reactivity but comparatively lower stability. The topological analyses, including ELF and LOL, confirm the presence of both localized and delocalized electron density regions within the molecular frameworks. Meanwhile, the RDG–NCI analysis reveals red regions embedded within the quinolone and piperazine rings, indicative of steric repulsion, while green patches located near the methyl (CH_3), carboxyl (COOH), and methylene (CH_2) groups highlight the existence of stabilizing van der Waals interactions. However, molecular docking studies demonstrate that the chlorinated derivative ECMPQC exhibits stronger binding affinity toward the target proteins, which can be attributed to the larger atomic size, higher polarizability, and increased hydrophobic nature of chlorine, leading to enhanced ligand–protein interactions. Overall, EFMPQC is more suitable for applications requiring high stability and favorable electronic properties, whereas ECMPQC appears more promising for applications involving strong biological interactions, such as drug–receptor binding and antiviral drug design.

References

[1] D. Benedetto Tiz, L. Bagnoli, O. Rosati, F. Marini, L. Sancineto, C. Santi, New halogen-containing drugs approved by FDA in 2021: An overview on their syntheses and pharmaceutical use. Molecules, 27(5), (2022) 1643. https://doi.org/10.3390/molecules27051643v

[2] Z. Xu, Z. Yang, Y. Liu, Y. Lu, K. Chen, W. Zhu, Halogen bond: its role beyond drug–target binding affinity for drug discovery and development. Journal of Chemical Information and Modeling, 54(1), (2014) 69-78. https://doi.org/10.1021/ci400539q

[3] M.Z. Hernandes, S.M.T. Cavalcanti, D.R.M. Moreira, W.F. de Azevedo Junior, A.C.L. Leite, Halogen atoms in the modern medicinal chemistry: hints for the drug design. Current Drug Targets, 11(3), (2010) 303-314. http://dx.doi.org/10.2174/138945010790711996

[4] H. Mei, J. Han, S. Fustero, M. Medio-Simon, D.M. Sedgwick, C. Santi, R. Ruzziconi, V.A. Soloshonok, Fluorine-containing drugs approved by the FDA in 2018. Chemistry–A European Journal, 25(51), (2019) 11797-11819. https://doi.org/10.1002/chem.201985161

[5] K.L. Kirk, Fluorine in medicinal chemistry: Recent therapeutic applications of fluorinated small molecules. Journal of Fluorine Chemistry, 127(8), (2006) 1013-1029. https://doi.org/10.1016/j.jfluchem.2006.06.007

[6] C. Isanbor, D. O'Hagan, Fluorine in medicinal chemistry: A review of anti-cancer agents. Journal of Fluorine Chemistry, 127(3), (2006) 303-319. https://doi.org/10.1016/j.jfluchem.2006.01.011

[7] N. Sheikhi, M. Bahraminejad, M. Saeedi, S.S. Mirfazli, A review: FDA-approved fluorine-containing small molecules from 2015 to 2022. European Journal of Medicinal Chemistry, 260, (2023)115758. https://doi.org/10.1016/j.ejmech.2023.115758

[8] W.Y. Fang, L. Ravindar, K.P. Rakesh, H.M. Manukumar, C.S. Shantharam, N.S. Alharbi, H.L. Qin, Synthetic approaches and pharmaceutical applications of chloro-containing molecules for drug discovery: A critical review. European Journal of Medicinal Chemistry, 173, (2019)117-153. https://doi.org/10.1016/j.ejmech.2019.03.063

[9] J.G. Topliss, Utilization of operational schemes for analog synthesis in drug design. Journal of Medicinal Chemistry, 15(10), (1972) 1006-1011. https://doi.org/10.1021/jm00280a002

[10] J.G. Topliss, A manual method for applying the Hansch approach to drug design. Journal of Medicinal Chemistry, 20(4), (1977) 463-469. https://doi.org/10.1021/jm00214a001

[11] D. Chiodi, Y. Ishihara, "Magic chloro": profound effects of the chlorine atom in drug discovery. Journal of Medicinal Chemistry, 66(8) (2023) 5305-5331, https://doi.org/10.1021/acs.jmedchem.2c02015

[12] D.G. Brown, M.M. Gagnon, J. Bostrom, Understanding our love affair with p-chlorophenyl: present day implications from historical biases of reagent selection. Journal of Medicinal Chemistry, 58(5) (2015) 2390-2405, https://doi.org/10.1021/jm501894t

[13] S. Joshi, R. Srivastava, Effect of "Magic Chlorine" in drug discovery: an in silico approach. *RSC Advances*, *13*(49) (2023) 34922-34934, https://doi.org/10.1039/D3RA06638J.

[14] I. Vicenti, M. Zazzi, F. Saladini, SARS-CoV-2 RNA-dependent RNA polymerase as a therapeutic target for COVID-19. Expert Opinion

on Therapeutic Patents, 31(4) (2021) 325-337, https://doi.org/10.1080/13543776.2021.1880568

[15] S. Ullrich, C. Nitsche, The SARS-CoV-2 main protease as drug target. Bioorganic & Medicinal Chemistry Letters, 30(17) (2020) 127377, https://doi.org/10.1016/j.bmcl.2020.127377

[16] R.S. Keri, S.A. Patil, Quinoline: A promising antitubercular target. Biomedicine & Pharmacotherapy, 68(8) (2014) 1161-1175, https://doi.org/10.1016/j.biopha.2014.10.007

[17] A. Dorababu, Quinoline: A promising scaffold in recent antiprotozoal drug discovery. Chemistry Select, 6(9) (2021) 2164-2177, https://doi.org/10.1002/slct.202100115

[18] R. Musiol, J. Jampilek, V. Buchta, L. Silva, H. Niedbala, B. Podeszwa, A. Palka, K. Majerz-Maniecka, B. Oleksyn, J. Polanski, Antifungal properties of new series of quinoline derivatives. Bioorganic & Medicinal Chemistry, 14(10) (2006) 3592-3598. https://doi.org/10.1016/j.bmc.2006.01.016

[19] M.Y. Wang, R. Zhao, L.J. Gao, X.F. Gao, D.P. Wang, J.M. Cao, SARS-CoV-2: structure, biology, and structure-based therapeutics development. Frontiers in Cellular and Infection Microbiology, 10 (2020) 587269, https://doi.org/10.3389/fcimb.2020.587269

[20] V. Arjunan, P. Ravindran, T. Rani, S. Mohan, FTIR, FT-Raman, FT-NMR, ab initio and DFT electronic structure investigation on 8-chloroquinoline and 8-nitroquinoline. Journal of Molecular Structure, 988(1-3) (2011) 91-101, https://doi.org/10.1016/j.molstruc.2010.12.032

[21] A. Komasa, M. Szafran, A. Katrusiak, K. Roszak, Z. Dega-Szafran, Crystal and molecular structure of 8-hydroxyquinoline betaine monohydrate studied by X-ray, FTIR, NMR and DFT. Journal of Molecular Structure, 1248 (2022) 131421, https://doi.org/10.1016/j.molstruc.2021.131421

[22] M. Kumru, A. Altun, M. Kocademir, V. Kucuk, T. Bardakçı, I. Sasmaz, Combined experimental and quantum chemical studies on spectroscopic (FT-IR, FT-Raman, UV–Vis, and NMR) and structural characteristics of quinoline-5-carboxaldehyde. Journal of Molecular Structure, 1125 (2016) 302-309, https://doi.org/10.1016/j.molstruc.2016.06.066

[23] M. Kumru, V.E.S.I.L.E. Kucuk, M. Kocademir, H.M. Alfanda, A. Altun, L. Sarı, Experimental and theoretical studies on IR, Raman, and UV–Vis spectra of quinoline-7-carboxaldehyde. Spectrochimica Acta Part A: Molecular and Biomolecular Spectroscopy, 134 (2015) 81-89, https://doi.org/10.1016/j.saa.2014.06.094

[24] R. Thirumurugan, K. Raju, K. Moovendaran S. Raju, E. Shobhana, Exploring Second-Order Nonlinear Optical Performance in Oxyquinolinium 3-Carboxypropanoate: A Combined Experimental and DFT Study. International Research Journal of Multidisciplinary Technovation, 7(6) (2025) 191-211. https://doi.org/10.54392/irjmt25612

[25] S. Kavi Karunya, K. Jagathy, K. Anandaraj, C. Pavithra, R. Manjula, Exploration of Solvent Effects, Structural and Spectroscopic Properties, Chemical Shifts, Bonding Nature, Reactive Sites and Molecular Docking Studies on 3-Chloro-2,6-Difluoropyridin-4-Amine As a Potent Antimicrobial Agent. International Research Journal of Multidisciplinary Technovation, 6 (1) (2024) 109-27, https://doi.org/10.54392/irjmt2419

[26] M.J. Frisch, et al., Gaussian 09, Gaussian Inc, Wallingford CT, 2009, https://doi.org/10.1016/j.molstruc.2024.140062

[27] A.D. Becke, Density functional thermo chemistry – I: The effect of the exchange only gradient correlation, Journal of Chemical Physics, 98 (1993) 5648-5652, https://doi.org/10.1063/1.462066

[28] C. Lee, W. Yang, R.G. Parr, Development of the Colle-Salvetti correlation-energy formula into a functional of the electron density, Physical Review B, 37 (1988) 785-789.

[29] B. Miehlich, A. Savin, H. Stoll, H. Preuss, Results obtained with the correlation energy density functional of Becke and Lee, Yang and Parr, Chemical Physics Letters. 157 (3) (1989) 200-206.

[30] W. Kohn, L.J. Sham, Self-consistent equations including exchange and correlation effects, Physical Reiew, 140 (1965) A1133-A1138, https://doi.org/10.1103/PhysRev.140.A1133

[31] R. G. Parr and W. Yang, Density-functional theory of atoms and molecules (Oxford Univ. Press, Oxford, 1989).

[32] P. Hohenberg and W. Kohn, “Inhomogeneous Electron Gas,” Physical Reiew,136 (1964) B864-B71. DOI: https://doi.org/10.1103/PhysRev.136.B864

[33] R. Dennington, T.A. Keith, J.M. Millam GaussView 6.0. Semichem Inc., Shawnee Mission, KS, USA (2016).

[34] M. Petersilka, U.J. Gossman, E.K.U. Gross, Excitation energies from timedependent density-functional theory, Physical Reiew Letters, 76 (1996) 1212-1215, https://doi.org/10.1103/PhysRevLett.76.1212

[35] E. Runge, E.K.U. Gross, Density functional theory for time-dependent systems, Physical Reiew Letters, 52 (1984) 997, https://doi.org/10.1103/PhysRevLett.52.997

[36] R. Bauernschmitt, R. Ahlrichs, Treatment of electronic excitations within the adiabatic approximation of time-dependent density functional theory, Chemical Physics Letters. 256 (1996) 454-464. https://doi.org/10.1016/0009-2614(96)00440-X

[37] N.M. O'Boyle, A.L. Tenderholt, K.M. Langner. Journal of Computational Chemistry, 2008, 29, 839-845.

[38] E.D. Glendening, A.E. Reed, J.E. Carpenter, F. Weinhold, NBO Version 3.1, TCI, University of Wisconsin, Madison, 1998.

[39] G.A. Zhurko and D.A. Zhurko, Chemcraft Program Version 1.6 (Build 315), (2009) http://www.chemcraftprog.com

[40] T. Lu, F. Chen, Multiwfn: a multifunctional wavefunction analyzer, Journal of Computational Chemistry, 33 2012 580-592. https://doi.org/10.1002/jcc.22885

[41] G.M. Morris, R. Huey, W. Lindstrom, M.F. Sanner, R.K. Belew, D.S. Goodsell, A.J. Olson, AutoDock4 and AutoDockTools4: Automated docking with selective receptor flexibility, Journal of Computational Chemistry, 30 (2009) 2785-2791, https://doi.org/10.1002/jcc.21256

[42] W.L. DeLano, Pymol: an open-source molecular graphics tool. CCP4 Newsletter on protein Crystallography, 40(1) (2002) 82–92, http://www.pymol.org.

[43] A.C. Wallace, R.A. Laskowski, J.M. Thornton, LIGPLOT: a program to generate schematic diagrams of protein–ligand interactions, Protein Engineering, 8 (1995) 127–134, https://doi.org/10.1093/protein/8.2.127

[44] S. Badoglu, S. Yurdakul, FT-IR spectroscopic and dft computational study on solvent effects on 8-hydroxy-2-quinolinecarboxylic acid. Optics and Spectroscopy, 118 (2015) 364-388, https://doi.org/10.1134/S0030400X15030066

[45] R. Kanimozhi, V. Arjunan, S. Mohan, Conformations, structure, vibrations, chemical shift and reactivity properties of isoquinoline–1–carboxylic acid and isoquinoline–3–carboxylic acid–Comparative investigations by experimental and theoretical techniques. Journal of Molecular Structure, 1207 (2020) 127841, https://doi.org/10.1016/j.molstruc.2020.127841

[46] R.T. Ulahannan, C.Y. Panicker, H.T. Varghese, C. Van Alsenoy, R. Musiol, J. Jampilek, P.L. Anto, Spectroscopic (FT-IR, FT-Raman) investigations and quantum chemical calculations of 4-hydroxy-2-oxo-1, 2-dihydroquinoline-7-carboxylic acid. Spectrochimica Acta Part A: Molecular and Biomolecular Spectroscopy, 121, (2014) 404-414, https://doi.org/10.1016/j.saa.2013.10.114.

[47] V. Vijayalakshmi, N. Kanagathara, J. Jan, M.K. Marchewka, A. Mohammad, K. Senthilkumar, Structural, spectroscopic and second harmonic generation evaluation of 1, 2, 4-triazolinium tartrate-tartaric acid as a promising nonlinear optical material, Optical Materials, 147 (2024) 11469. https://doi.org/10.1016/j.optmat.2023.114694

[48] C.C. Sangeetha, R. Madivanane, V. Pouchaname, The vibrational spectroscopic (FT-IR & FTR) study and HOMO & LUMO analysis of 6-methyl quinoline using DFT studies. Archives of Physics Research, 4(3) (2013) 67-77.

[49] N. Sundaraganesan, E. Kavitha, S. Sebastian, J.P. Cornard, M. Martel, Experimental FTIR, FT-IR (gas phase), FT-Raman and NMR spectra, hyperpolarizability studies and DFT calculations of 3, 5-dimethylpyrazole. Spectrochimica Acta Part A: Molecular and Biomolecular Spectroscopy, 74(3) (2009) 788-797, https://doi.org/10.1016/j.saa.2009.08.019

[50] A. Ram Kumar, S. Selvaraj, A.S. Vickram, J. Jenifer, R.K. Raja, Experimental and theoretical investigations on antiproliferative compound nootkatone's vibrational characteristics, solvent effects of electronic properties, topological insights, Hirshfeld surface, donor-acceptor insights, ADME, and molecular docking against SMAD proteins. Journal of Molecular Structure, 1346 (2025) 143156, https://doi.org/10.1016/j.molstruc.2025.143156

[51] V. Udayakumar, S. Periandy, M. Karabacak, S. Ramalingam, Experimental (FT-IR, FT-Raman) and theoretical (HF and DFT) investigation and HOMO and LUMO analysis on the structure of p-fluoronitrobenzene. Spectrochimica Acta Part A: Molecular and Biomolecular Spectroscopy, 83(1) (2011) 575-586. https://doi.org/10.1016/j.saa.2011.09.008

[52] M. Karabacak, D. Karagoz, M. Kurt, Experimental (FT-IR and FT-Raman spectra) and theoretical (ab initio HF, DFT) study of 2-chloro-5-methylaniline. Journal of Molecular Structure, 892(1-3) (2008) 25-31, https://doi.org/10.1016/j.molstruc.2008.04.054

[53] N. Sundaraganesan, B. Anand, C. Meganathan, B.D. Joshua, FT-IR, FT-Raman spectra and ab initio HF, DFT vibrational analysis of 2, 3-difluoro phenol. Spectrochimica Acta Part A: Molecular and Biomolecular Spectroscopy, 68(3) (2007) 561-566, https://doi.org/10.1016/j.saa.2006.12.028

[54] P. Divya, V.J. Reeda, S. Selvaraj, B. Jothy, Theoretical spectroscopic electronic elucidation with polar and nonpolar solvents (IEFPCM model), molecular docking and molecular dynamic studies on bendiocarb-antiallergic drug agent. Journal of Molecular Liquids, 404 (2024) 124895, https://doi.org/10.1016/j.molliq.2024.124895

[55] P. Divya, V.J. Reeda, S. Renuga, C.D. Annapoorani, V.B. Jothy, Vibrational analysis, DFT computations of spectroscopic, non-covalent analysis with molecular docking and dynamic simulation of 2-amino-4, 6-dimethyl pyrimidine benzoic acid, Journal of Molecular Structure, 1318 (2024) 139160, https://doi.org/10.1016/j.molstruc.2024.139160

[56] A, Mani, R. Elaiyaraja, Taurolidine, a Sulfonic Amino Acid Derivative, Induces Apoptosis and Cytotoxicity Against Cervical Cell Carcinoma an In Silico and in Vitro Approach, International Research Journal of Multidisciplinary Technovation, 7 (4) (2025) 70-81. https://doi.org/10.54392/irjmt2546

[57] E. Mohanapriya, S. Elangovan, N. Kanagathara, M.K. Marchewka, J. Janczak, P. Revathi, P, Density functional theory calculations, structural and spectroscopic characterization, and solvent-dependent HOMO-LUMO studies of 2-nitro-4-methylanilinium benzenesulfonate. Journal of

Molecular Structure, 1317 (2024) 139147, https://doi.org/10.1016/j.molstruc.2024.139147

[58] S. Akshay Kalyan, N. Kanagathara, M.K. Marchewka, J. Janczak, K. Senthilkumar, Structure, Spectroscopy, and Theoretical insights on Co-crystals of 2, 4-Diamino-6-Methyl-1, 3, 5-Triazine Bis (4-Aminobenzoic acid) Monohydrate as a promising anti-cancer agent. Physica B: Condensed Matter, 679 (2024) 415807, https://doi.org/10.1016/j.physb.2024.415807

[59] K.A. Peele, C.P. Durthi, T. Srihansa, S. Krupanidhi, V.S. Ayyagari, D.J. Babu, M. Indira, A.R. Reddy, T.C. Venkateswarulu, Molecular docking and dynamic simulations for antiviral compounds against SARS-CoV-2: A computational study. Informatics in Medicine Unlocked, 19 (2020) 100345, https://doi.org/10.1016/j.imu.2020.100345

[60] W.S. Qayed, R.S. Ferreira, J.R.A. Silva, In silico study towards repositioning of FDA-approved drug candidates for anticoronaviral therapy: Molecular docking, molecular dynamics and binding free energy calculations. Molecules, 27(18) (2002) 5988, https://doi.org/10.3390/molecules27185988

Authors Contribution Statement

A. Ram Kumar: Writing – Original draft, Conceptualization, Data Curation, Validation, Investigation. A. S. Vickram: Supervision, Visualization, Validation, Resources. J. Jenifer: Data curation, Formal analysis, Validation. S. Selvaraj: Writing – Review & Editing, Supervision, Conceptualization, Methodology, Investigation. All the authors read and approved the final version of the manuscript.

Funding

The authors declare that no funds, grants or any other support were received during the preparation of this manuscript.

Competing Interests

The authors declare that there are no conflicts of interest regarding the publication of this manuscript.

Data Availability

The data supporting the findings of this study can be obtained from the corresponding author upon reasonable request.

Has this article screened for similarity?

Yes

About the License